AGU PUBLICATIONS

JGR

Journal of Geophysical Research: Planets

RESEARCH ARTICLE
10.1002/2014JE004784

Key Points:
- Amorphous iron sulfates are spectrally characterized
- Amorphous ferric sulfates could form from brines on Mars
- Amorphous ferric sulfates precipitated onto basalt spectrally resemble basalt

Supporting Information:
- Supporting Information S1

Correspondence to:
E. C. Sklute,
ecsklute@mtholyoke.edu

Citation:
Sklute, E. C., H. B. Jensen, A. D. Rogers, and R. J. Reeder (2015), Morphological, structural, and spectral characteristics of amorphous iron sulfates, *J. Geophys. Res. Planets*, *120*, 809–830, doi:10.1002/2014JE004784.

Received 27 DEC 2014
Accepted 19 MAR 2015
Accepted article online 25 MAR 2015
Published online 30 APR 2015

Morphological, structural, and spectral characteristics of amorphous iron sulfates

E. C. Sklute[1,2], H. B. Jensen[1], A. D. Rogers[1], and R. J. Reeder[1]

[1]Department of Geosciences, State University of New York at Stony Brook, Stony Brook, New York, USA, [2]Now at Department of Astronomy, Mount Holyoke College, South Hadley, Massachusetts, USA

Abstract Current or past brine hydrologic activity on Mars may provide suitable conditions for the formation of amorphous ferric sulfates. Once formed, these phases would likely be stable under current Martian conditions, particularly at low- to mid-latitudes. Therefore, we consider amorphous iron sulfates (AIS) as possible components of Martian surface materials. Laboratory AIS were created through multiple synthesis routes and characterized with total X-ray scattering, thermogravimetric analysis, scanning electron microscopy, visible/near-infrared (VNIR), thermal infrared (TIR), and Mössbauer techniques. We synthesized amorphous ferric sulfates ($Fe(III)_2(SO_4)_3 \cdot \sim 6–8H_2O$) from sulfate-saturated fluids via vacuum dehydration or exposure to low relative humidity (<11%). Amorphous ferrous sulfate ($Fe(II)SO_4 \cdot \sim 1H_2O$) was synthesized via vacuum dehydration of melanterite. All AIS lack structural order beyond 11 Å. The short-range (<5 Å) structural characteristics of amorphous ferric sulfates resemble all crystalline reference compounds; structural characteristics for the amorphous ferrous sulfate are similar to but distinct from both rozenite and szomolnokite. VNIR and TIR spectral data for all AIS display broad, muted features consistent with structural disorder and are spectrally distinct from all crystalline sulfates considered for comparison. Mössbauer spectra are also distinct from crystalline phase spectra available for comparison. AIS should be distinguishable from crystalline sulfates based on the position of their Fe-related absorptions in the visible range and their spectral characteristics in the TIR. In the NIR, bands associated with hydration at ~1.4 and 1.9 μm are significantly broadened, which greatly reduces their detectability in soil mixtures. AIS may contribute to the amorphous fraction of soils measured by the Curiosity rover.

1. Introduction

A preponderance of evidence from recent orbital and landed missions points to the existence of hydrated sulfate phases on the Martian surface [*Johnson et al.*, 2007; *Lane et al.*, 2004, 2008; *Lichtenberg et al.*, 2010; *Milliken et al.*, 2009; *Roach et al.*, 2009, 2010a, 2010b; *Wang et al.*, 2013]. Some of those phases are likely hydrated iron sulfates [*Bishop et al.*, 2009; *Johnson et al.*, 2007; *Karunatillake et al.*, 2014; *Lane et al.*, 2004, 2008; *Lichtenberg et al.*, 2010; *Milliken and Bish*, 2010; *Roach et al.*, 2010a; *Wang et al.*, 2013; *Wiseman et al.*, 2010; *Wray et al.*, 2011]. Because iron sulfate structure and stability (including amorphous phases) are dependent upon relative humidity, temperature, fluid chemistry, and parent phases [*Xu et al.*, 2009], identification of specific iron sulfate phases has important implications for both surficial and atmospheric processes on Mars. The spectral characteristics of *crystalline* iron sulfates have been well characterized [*Cloutis et al.*, 2006; *Crowley et al.*, 2003; *Dyar et al.*, 2013; *Lane*, 2007; *Lane et al.*, 2015; *Majzlan and Michallik*, 2007; *Majzlan et al.*, 2005; *Wang et al.*, 2009]; however, limited work has been done to characterize the spectral, morphological, and structural characteristics of amorphous ferric and ferrous sulfate phases [*Burgina et al.*, 1996; *Lazaroff et al.*, 1982, 1985, 1998; *Margulis et al.*, 1975, 1976]. As described below, amorphous sulfate phases may be important components of Martian soils.

Amorphous iron sulfates have previously been shown to form via two broad mechanisms, both of which involve rapid dehydration. First, when $Fe(III)_2(SO_4)_3$-saturated fluids are subjected to low relative humidity ((RH) <11%), as one would expect on Mars under most conditions [*Audouard et al.*, 2014; *Harri et al.*, 2014; *Savijarvi*, 1995], amorphous ferric phases, rather than crystalline ferric phases, precipitate from the saturated fluids [*Wang et al.*, 2012; *Xu and Parise*, 2012; *Xu et al.*, 2009]. To date, amorphous ferrous sulfates have not been formed via this mechanism, despite experimental efforts to do so [*Altheide et al.*, 2009; *Wang and Zhou*, 2014]. Amorphous ferrous sulfates have been formed via the second mechanism, however, which is dehydration of crystalline hydrated ferrous sulfates (e.g., melanterite or rozenite) under Mars-relevant pressures and temperatures [*Wang and Zhou*, 2014].

Poorly crystalline but not fully amorphous sulfates have also been formed/observed in a variety of experimental studies. *Wang and Ling* [2011] report a "quasi-amorphous" phase made through vacuum dehydration of ferricopiapite, but this phase exhibited numerous XRD peaks indicating retention of some long-range crystalline structure. "Poorly crystalline sulfates" have also been observed in alteration assemblages during acid fog weathering of basalt [*Golden et al*., 2005; *Tosca et al*., 2004]. Structurally "disordered" Mg sulfate was generated from flash-freezing Mg sulfate brines [*McCord et al*., 2002]. Metastable "amorphous" hydroxysulfates (reported as either $Fe_4(SO_4)_2(OH)_{10}$ [*Burgina et al*., 1996] or $2Fe_2O_3 \cdot SO_3 \cdot XH_2O$ [*Lazaroff et al*., 1982, 1985, 1998; *Margulis et al*., 1975, 1976]) have been formed through the hydrolysis of $Fe_2(SO_4)_3$ solutions [*Burgina et al*., 1996; *Margulis et al*., 1975, 1976] and as a by-product of iron oxidation by *Thiobacillus Ferrooxidans* [*Lazaroff et al*., 1982, 1985, 1998]. It is unclear from the literature if these are, in fact, the same compound. The compound produced by hydrolysis may simply be aggregates of tetramers [*Burgina et al*., 1996], but the biogenic by-product is a fibrous polymer [*Lazaroff et al*., 1982, 1985, 1998] and may be a major constituent of acid mine drainage sediments [*Bigham et al*., 1990]. The detailed investigation by *Bigham et al*. [1990], however, showed that both formation mechanisms produce products that are merely poorly crystalline at the resolution of XRD, with a structure similar to the hydroxide akaganéite, and are thus not included in this study.

The recent discovery of a phenomenon known as recurring slope lineae [*McEwen et al*., 2011] points to an active present-day brine hydrologic cycle on Mars [*Altheide et al*., 2009; *Chevrier and Altheide*, 2008; *Martinez and Renno*, 2013; *Masse et al*., 2014; *McEwen et al*., 2011] that could create conditions appropriate for the formation of amorphous sulfates on the surface. Several salts that are present on Mars [*Gendrin et al*., 2005; *Squyres et al*., 2004; *Wang et al*., 2006b] create brines with eutectics below the freezing point of pure water [*Altheide et al*., 2009; *Brass*, 1980; *Chevrier and Altheide*, 2008; *Marion et al*., 2003; *Mohlmann and Thomsen*, 2011; *Sears and Chittenden*, 2005]. Brines can form any time the relative humidity of the atmosphere is above the deliquescence relative humidity of the salt. These brines are more stable in the subsurface because the RH is likely higher [*Wang et al*., 2012, 2013], and the upper soil layer protects against evaporation [*Chevrier et al*., 2007; *Chevrier and Altheide*, 2008]. However, these fluids will be subject to boiling if the atmospheric vapor pressure is below the saturation vapor pressure of the fluid and will be subject to evaporation any time the partial pressure of H_2O is below the saturation water vapor pressure for the fluid [*Martinez and Renno*, 2013]. On the surface, they are stable for only short periods of time and would likely boil or evaporate rapidly depending on latitude [*Chevrier and Altheide*, 2008]. Considering the experimental studies described above, we suggest that both of these phenomena (boiling or evaporation) could lead to formation of amorphous sulfates on Mars.

The stability of these amorphous phases, once formed, depends on RH and temperature conditions. A series of studies by A. Wang and collaborators and W. Xu and collaborators have investigated the phase transitions and stability of sulfate phases at Mars relevant temperatures and pressures. [*Chou et al*., 2013; *Kong et al*., 2011a, 2011b; *Ling and Wang*, 2010; *Wang and Ling*, 2011; *Wang et al*., 2006a, 2009, 2011, 2012, 2013]. For example, when solid amorphous ferric sulfates are kept at RH $< 11\%$ and 5°C, they will remain amorphous for at least 4 years (the length of the longest-term experiments) [*Wang et al*., 2012]. Increasing the temperature to 21°C causes the stability field for the amorphous phase to shift to lower relative humidity (RH $< 6\%$). Increasing relative humidity to 33% RH at 5°C causes the amorphous solid to increase its structural water content without immediately crystallizing, varying from 5 to 11 structural waters [*Wang et al*., 2012]. These studies imply that if amorphous ferric sulfates were to form on the surface of Mars, they may be able to persist as amorphous phases, enduring the diurnal RH fluctuations without crystallizing.

Although several previous studies have established the stability fields of sulfate systems under terrestrial and Martian conditions [*King and McSween*, 2005; *King et al*., 2004; *Shepard and Helfenstein*, 2007; *Vaniman and Chipera*, 2006; *Vaniman et al*., 2004; *Wang et al*., 2006a, 2009, 2011, 2012, 2013; *Xu and Parise*, 2012; *Xu et al*., 2009], and the spectral characteristics of crystalline sulfates are well documented [*Cloutis et al*., 2006; *Lane*, 2007; *Lane et al*., 2015], limited work has been done to characterize the amorphous phases [*Vaniman and Chipera*, 2006; *Vaniman et al*., 2004]. Here we report the morphological and spectroscopic characteristics of amorphous ferric and ferrous iron sulfates so that these observations can be added to spectral libraries to which we compare remotely acquired data. Accurate identification of these phases is critical for characterizing fluid compositions and conditions that produced hydrated phases on Mars, as well as the subsequent environmental conditions that may have modified crystalline sulfates.

2. Methods

For this work, amorphous ferric iron sulfates were synthesized from two starting materials: first using unaltered Acros Organics 97% $Fe(III)_2(SO_4)_3 \cdot 5H_2O$ (batch report shows 22.9% Fe, <0.01% HCl insoluble matter, <5 ppm As, 5 ppm Cu, <200 ppm Fe^{2+}, 18 ppm Zn, <50 ppm Cl, <200 ppm NO_3, <30 ppm PO_4, and 0.03% SO_4), identified by XRD to be the monoclinic phase lausenite $(Fe(III)_2(SO_4)_3 \cdot 6H_2O)$; second by heating the Acros starting material for 2 h at 350°C to form the anhydrous trigonal phase mikasaite $(Fe(III)_2(SO_4)_3$; confirmed by XRD) [*Xu et al.*, 2009]. Although the starting material only reports 97% purity, additional experiments were performed with Alfa Aesar Puratronic (99.998%) ferric sulfate starting material (results not shown) and all spectral results were found to be identical, indicating none of the spectral features come from the impurities within the sample. Results for the Puratronic material are not reported because it was not a naturally occurring sulfate phase.

Both starting materials were placed in enclosures maintained at 92% relative humidity (RH) at ambient temperature (confirmed by RH probe), using de-ionized water as a humidity buffer. Once deliquesced, the materials were dehydrated via two methods: either by using low RH (11% by LiCl buffer) [*Xu et al.*, 2009] or by vacuum (3×10^{-2} mbar; Edwards E2M2 vacuum pump attached to an Applied Vacuum Engineering VF range bell jar). Both of these methods simulate the rapid loss of water that brines would likely experience once exposed on the Martian surface; dehydration in low RH simulates evaporation, whereas vacuum desiccation simulates boiling. These samples will be referred to as LV-amorphous, LH-amorphous, MV-amorphous, and MH-amorphous to reflect their starting materials of lausenite (L) and mikasaite (M), as well as their dehydration method of vacuum (V) or humidity buffer (H). Amorphous ferrous sulfate was prepared by vacuum dehydrating melanterite (Alfa Aesar 99 + % iron sulfate heptahydrate; $FeSO_4 \cdot 7H_2O$) for 3 days (phase purity confirmed by XRD; when necessary, the reagent was rehydrated in 92% RH chamber before beginning dehydration or analyses and analyses were performed at high relative humidity). This synthesis method was based on a published method for obtaining amorphous Mg sulfate from hexahydrate [*Vaniman et al.*, 2004].

The materials were confirmed amorphous at the resolution of XRD using a Scintag PAD X powder diffractometer (Cu Kα radiation; 25 mA; 45 kV). Once created, the ferric sulfates were kept at low RH (less than 11%) except during spectral analyses (<20 min). Lack of crystallinity was checked by XRD after each analysis. Because these phases lack long-term stability in Earth's atmosphere [*Ling and Wang*, 2010; *Xu et al.*, 2009], the reproducibility of the synthesis methods was confirmed through repeated synthesis and subsequent spectral analysis. This procedure allowed for a fresh sample to be produced for each measurement rather than using the same sample after exposure to ambient and/or experimental conditions. Overlapping measurements were periodically taken to ensure that the above assumption remained valid.

Visible/near-infrared reflectance (VNIR) spectra were collected on an ASD inc. (a PANalytic company) Fieldspec3 Max ultraviolet-visible-near infrared (UV-VIS-NIR) bidirectional spectrometer (referenced to Spectralon; average of 300 scans) in the Vibrational Spectroscopy Laboratory (VSL) at the State University of New York at Stony Brook. When laboratory humidity exceeded 15% (monitored by RH probe), VNIR spectra were collected in an N_2 filled glove bag. Spectral emissivity measurements, also taken at VSL, were acquired on a Nicolet 6700 Fourier transform infrared (FTIR) spectrometer custom modified to collect emitted energy. Spectra were acquired in a dry air purged chamber and calibrated using blackbody targets at two different temperatures [*Ruff et al.*, 1997]. Spectra were only collected when laboratory humidity was less than 15% (melanterite, which is only stable at high relative humidity was the exception and was analyzed on a humid day). To avoid phase changes that could occur upon heating, the samples were cooled and held at −10°C, approximately 30° below the room temperature detector temperature (rather than heated above detector temperature), to achieve adequate signal-to-noise for spectral measurement [*Baldridge and Christensen*, 2009]. Spectral emissivity measurements were taken on both powders and pressed pellets. Pellet measurements minimize spectral contributions from volume scattering [*Salisbury and Wald*, 1992]. To ensure that the pressure (3.5 t) did not introduce crystallinity, XRD patterns were collected from the pellets before and after emissivity measurements and compared to those for fresh, powdered samples. Thermogravimetric analysis (TGA), using a Netzsch STA Jupiter simultaneous TG-DSC apparatus, was used to determine sample H_2O contents (standard error calculated at 0.1%). Scanning Electron Microscopy (SEM) was used to image sample morphologies.

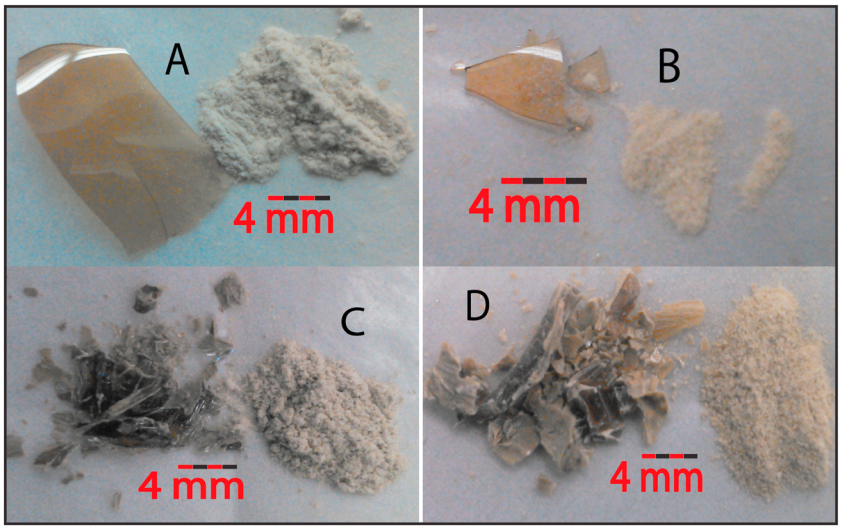

Figure 1. Image of partially ground, amorphous ferric sulfates: (a) LH amorphous, (b) MH amorphous, (c) LV amorphous, and (d) MV amorphous.

Synchrotron X-ray total scattering data were collected at beamline 11-ID-B at the Advanced Photon Source, Argonne National Laboratory, using a monochromatic X-ray beam (~58 keV, $\lambda = 0.2127$ Å) of approximately 500 μm diameter. Samples were loaded into Kapton capillaries, approximately 1 mm in diameter. The total scattering experiment is well described by *Billinge and Kanatzidis* [2004] and *Reeder and Michel* [2013]. Briefly, the total scattering experiment refers to the collection of both the elastic Bragg and the diffuse scattering components from a sample subjected to X-ray radiation. Total scattering experiments using conventional X-ray sources are of limited value for two reasons: first, the real space resolution is proportional to the range of angles over which data can be collected, which is, in turn, dependent upon the energy of the X-rays; and second, the intensity of the diffuse component is much less intense than the Bragg component, requiring higher photon fluxes for adequate signal. The high-energy synchrotron X-ray source allows measurements to be made to a much higher scattering angle and provides greatly increased flux, compared to a conventional source. After the scattering data are normalized and corrected for instrumental factors, the reduced structure function is Fourier transformed to give the pair distribution function (PDF), which is the distribution of interatomic distances of the material weighted by the scattering power of the atoms. The PDF provides direct structural information over a range of length scales, for crystalline and amorphous solids.

Mössbauer spectra were collected at Mount Holyoke College on a Web Research Co. (now See Co.) W100 spectrometer using a ~80 mCi ^{57}Co source in rhodium. Spectra were calibrated to α-Fe foil. Run times ranged from 2 to 12 h. Mössbauer data were fit using Mexfieldd, a program provided by E. DeGrave at the University of Ghent, Belgium. The program solves the full hyperfine interaction Hamiltonian to fit Lorentzian doublets to the spectral data with isomer shift (δ), quadrupole splitting (Δ), and full width at half maximum (Γ) as free parameters [*Degrave and Vanalboom*, 1991; *Vandenberghe et al*., 1994].

3. Results

3.1. General Observations

When precipitated in low humidity or under vacuum, and processed in a low humidity environment after synthesis, amorphous ferric sulfates form as amber-colored, translucent solids that grind into fine, ocher-white powders (Figure 1). X-ray diffraction patterns of the solids and powders lack sharp peaks and display only a slight swell in the baseline centered around 26° 2θ (Figure 2). Therefore, both the solid and powdered forms can be designated XRD amorphous. Upon dehydration, ferrous sulfates transform into a silky gray powder, the grains of which maintain the shape of the crystals from which they formed (Figure 3). The ferrous sulfates display a similar XRD pattern with a swell centered around 29° 2θ and thus is also designated XRD amorphous (Figure 2). Although extensive stability studies have not been performed for the purpose of

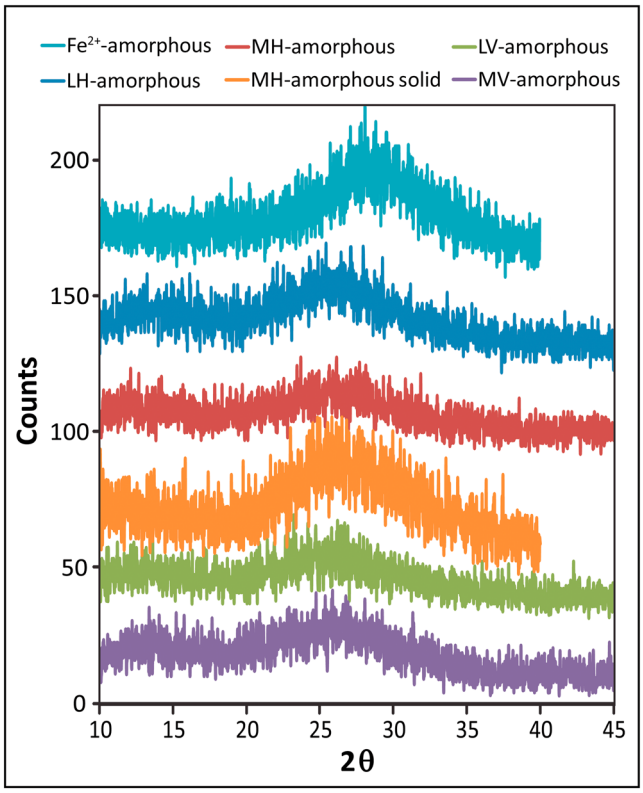

Figure 2. XRD patterns of amorphous ferric and ferrous sulfates. All XRD patterns are of powders except where indicated; "solid" refers to the amber chip seen in Figure 1b. All samples were run on a zero background plate.

this work, as such studies have been reported elsewhere [e.g., *Wang et al.*, 2012], a few general stability trends for the amorphous ferrous and ferric sulfates can be noted. The amorphous ferrous sulfates are less stable than the amorphous ferric sulfates under ambient conditions. Upon exposure to ambient temperatures (~23°C) and 14% RH, amorphous ferrous sulfates begin to turn from silver to gray over the course of 24 h and begin to show the emergence of sharp peaks in the XRD pattern after 48 h. The amorphous ferric sulfates, on the other hand, remain XRD amorphous for days, slowly taking on a surface coating of liquid water before finally beginning to crystallize. Under ambient temperatures (~23°C) and 35–55%RH, the amorphous ferrous sulfates begin to crystallize within minutes and the amorphous ferric sulfates within hours to a day, but amorphous ferric sulfates always form a surface coating of liquid water before crystallizing.

3.2. Morphology, Hydration State, and Range of Structural Order

SEM investigations show that the amorphous ferric sulfates display conchoidal fracture (Figure 4). SEM micrographs of the amorphous ferrous sulfate show that the crystals of melanterite have thin lamellar separation, yet they remain intact (Figure 5, left). Magnification shows that the microstructure appears to be sheets, which break into platelets when ground (Figure 5, right). This fracture pattern is consistent with melanterite's structure, which consists of isolated octahedra and tetrahedra connected through hydrogen bonding to the structural waters in alternating layers. The rapid dehydration appears to separate some of the layers.

TGA data (included as supporting information) were acquired to determine the number of structural waters of the amorphous samples and to provide normalization for PDF analysis (section 2.0). The TGA curves for the amorphous ferric sulfate samples show a gradual weight loss to ~150°C followed by a steeper loss to ~200°C. The slope of the TGA curves becomes gradual again by 250°C. This is interpreted as the loss of loosely bound and adsorbed water followed by the loss of structural water [*Knowlton et al.*, 1981]. The TGA curve for the amorphous ferrous sulfate sample is almost level to ~133°C followed by a steep decrease to ~250°C, after which the slope becomes gradual again. This is interpreted as the loss of structural water from a single energetic environment. Similar TGA curves have been reported for other iron sulfates [*McAdam et al.*, 2014]. At 250°C, the amorphous ferric sulfates had transformed into mikasaite, and amorphous ferrous

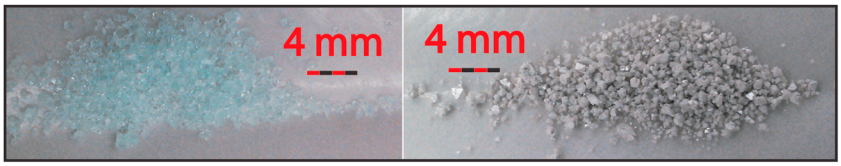

Figure 3. Image of (left) starting melanterite and (right) vacuum-dehydrated amorphous ferrous sulfate.

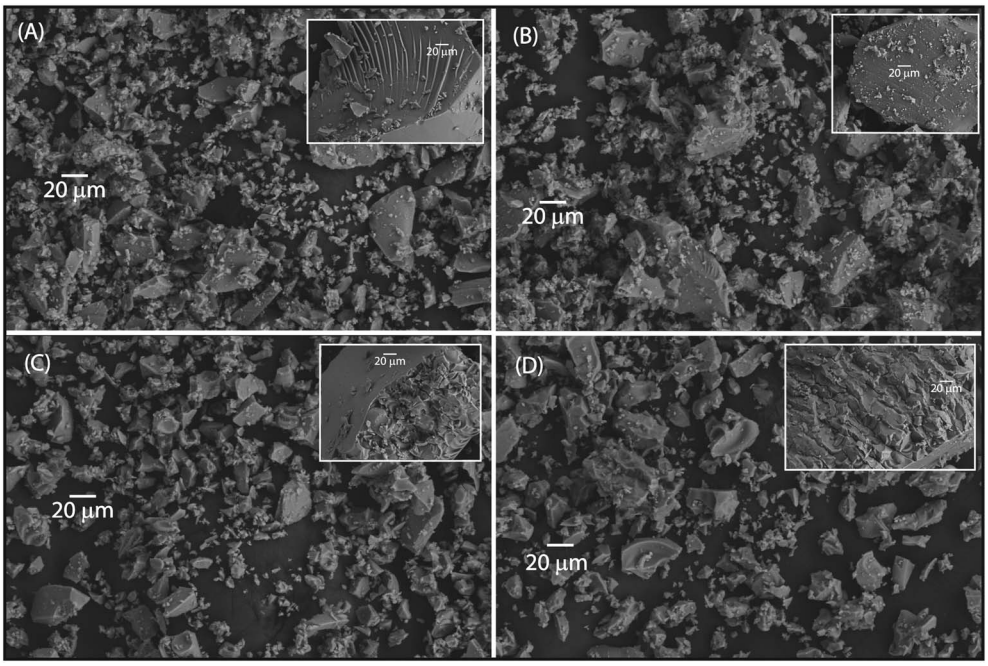

Figure 4. SEM images of (a) the LH-amorphous sample, (b) the MH-amorphous sample, (c) the LV-amorphous sample, and (d) the MV-amorphous sample. The main images are of the finest ground sections used for PDF. Insets are of minimally ground sections used for XRD.

sulfate had transformed into anhydrous ferrous sulfate (confirmed through XRD). LV-amorphous sulfate contained a total (structural and adsorbed) of 7.4 water molecules (per $Fe_2(SO_4)_3$ structural unit), where MV-amorphous sulfate contained only 6.3. LH-amorphous sulfate contained 8.5 water molecules and MH-amorphous contained 8.2. The ferrous sulfate sample contained 0.97 water molecules (per $FeSO_4$ structural unit).

Figure 6 shows the PDF for MV-amorphous sulfate overlaid on those of crystalline sulfates: ferricopiapite, lausenite, and mikasaite, for reference. Lausenite is the Acros reagent and mikasaite and ferricopiapite were synthesized from lausenite as part of this study. The corresponding reduced structure functions, Q(S(Q)-1), are shown in supporting information. The PDFs for the two crystalline phases display sharp peaks that extend beyond 50 Å (Figure 6, top), indicating that atom pair correlations exceed unit cell size. This type of PDF pattern is consistent with long-range structural order. The overall damping of peak intensity with increasing distance is characteristic of the experimental method, resulting from

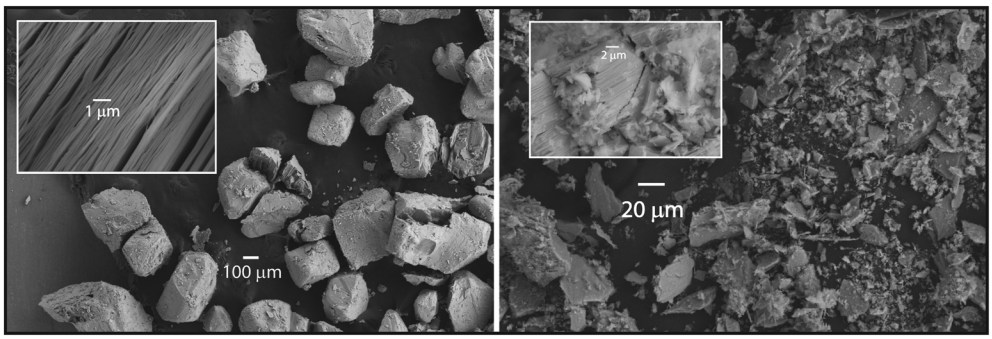

Figure 5. SEM images of (left) unground and (right) ground amorphous ferrous sulfate. Insets show layered structure likely resulting from rapid removal of interlayer water.

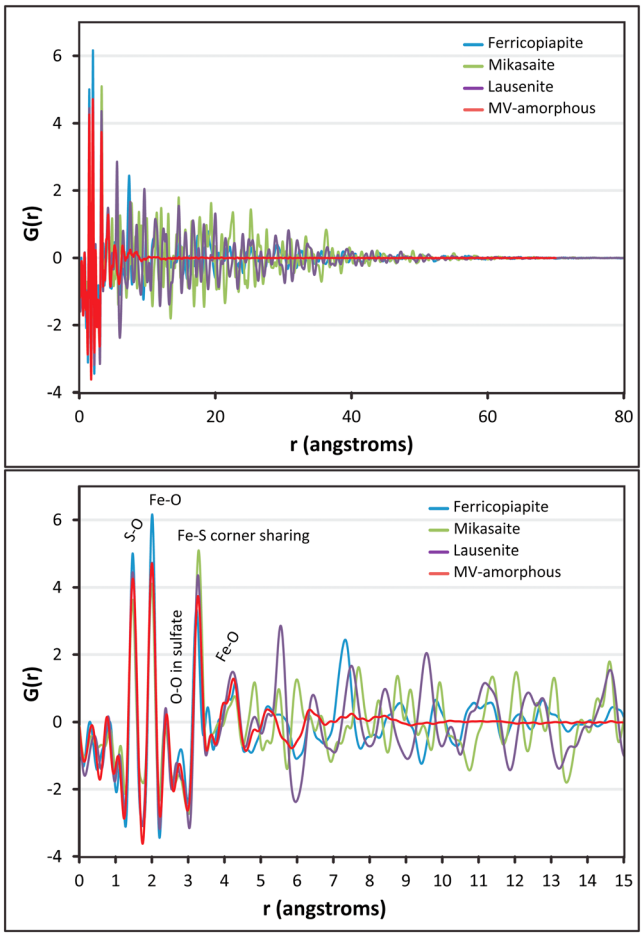

Figure 6. Pair distribution function of MV-amorphous ferric sulfate overlaid on the PDFs of crystalline ferricopiapite, lausenite, and mikasaite. (top) The expanded data range and (bottom) a close up at low *r*. Lausenite is the Acros reagent, and mikasaite and ferricopiapite were synthesized from lausenite as part of this study.

limitations in instrumental resolution. For the amorphous sample, however, no peaks are observed beyond ~10 Å (Figure 6, bottom), indicating no atom pair correlations beyond that point. Although SEM cannot provide sufficient resolution to definitively demonstrate that particle size is not on the order of 1 nm, the smooth surfaces seen in the SEM images (Figure 4) strongly suggest that particle size does not limit the length scale of pair correlations in the PDF to 10 Å. And while it is possible that aggregates could appear smooth at the resolution of SEM, it seems unlikely that no textural effects would be observed. Hence, the PDF results confirm the presence of short- and medium-range order (as represented by the peaks at low *r*) and the absence of long-range order, characteristic of amorphous solids.

It is notable that peaks in the amorphous ferric sample at ~4.3 Å and lower coincide in position with those of the crystalline ferric sulfates but of slightly lower intensity. These peaks correspond to the S-O bond in the sulfate group at ~1.48 Å, the first-shell Fe-O bond at ~2.00 Å, and the Fe-S distance corresponding to corner-shared SO_4 tetrahedra and Fe(III) octahedra at ~3.2–3.3 Å [cf. *Majzlan et al.*, 2006]. The composite peak centered at 4.2 Å corresponds to the distribution of Fe-O distances to corners of sulfate tetrahedra [cf. *Majzlan et al.*, 2006]. The correspondence of these distances to those in crystalline phases is not surprising, given that coordination between Fe(III) octahedra and sulfate tetrahedra is exclusively corner sharing in known mineral structures [*Hawthorne et al.*, 2000]. The lack of correspondence for the peaks at higher *r* reflects the different arrangements of Fe polyhedra when ordered (in the crystalline phases) as opposed to disordered in the amorphous phase.

The PDFs for all four of the amorphous ferric samples are compared in Figure 7. The PDF for all four samples are similar, indicating that these samples share the same short- and medium-range structure and that they are all amorphous. Thus, different pathways in the formation of amorphous ferric sulfate lead to the same local structure.

The PDF for the amorphous ferrous sulfate sample is shown in Figure 8 overlaid on those for crystalline reference compounds szomolnokite and rozenite. Again, the PDFs for the crystalline phases show sharp peaks that extend beyond 50 Å, but the amorphous sample displays no peaks past ~11 Å (Figure 8, bottom), indicating that the amorphous ferrous sulfate lacks long-range structural order. Because SEM imaging for this sample also suggests that the particle size is larger than 11 Å, the PDF for the amorphous ferrous sulfate also indicates that it is an amorphous solid. The amorphous ferrous sulfate appears to have short-range order (<4 Å) that is similar to, yet distinct from, both szomolnokite and rozenite, specifically in the first shell Fe-O distance and in the region near 4 Å where second shell Fe-O distances occur in szomolnokite (this correlation occurs at greater distances in rozenite) (Figure 8, bottom). The amorphous ferrous sulfate

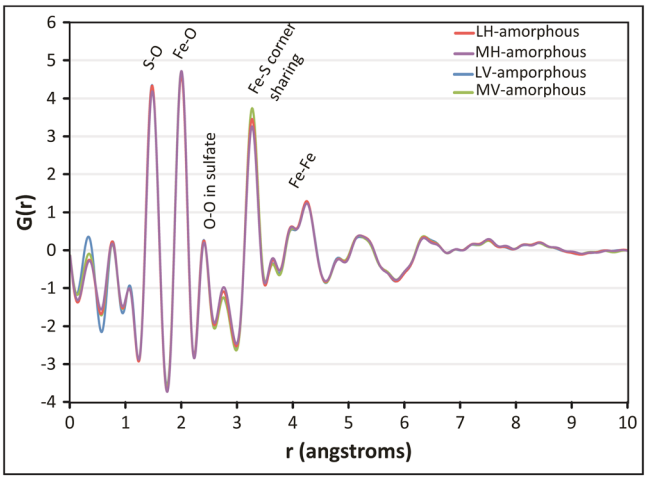

Figure 7. Pair distribution functions of the amorphous ferric sulfate samples.

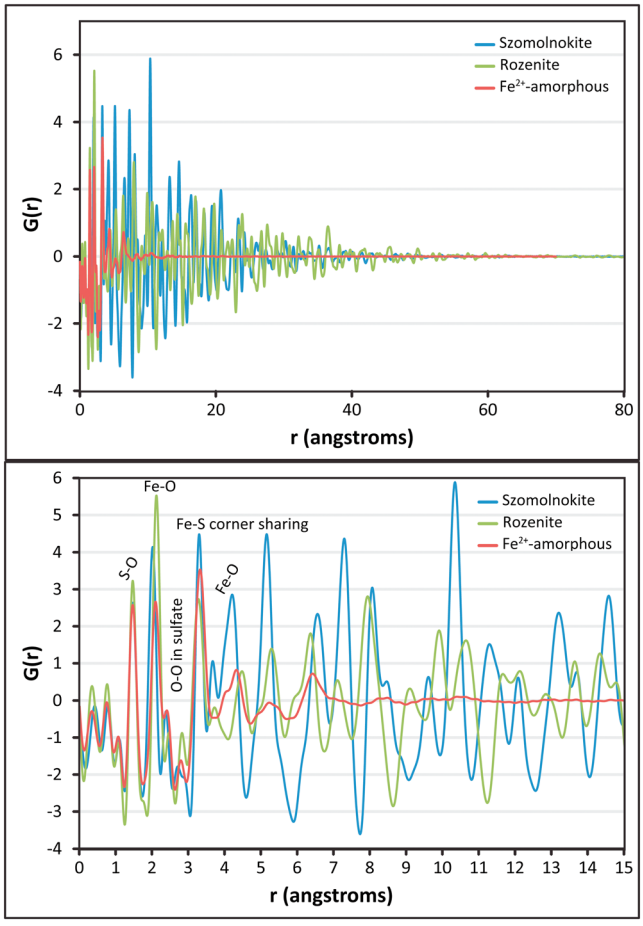

Figure 8. Pair distribution function of amorphous ferrous sulfate overlaid on the PDFs of crystalline szomolnokite and rozenite. (top) The expanded data range and (bottom) a close up at low *r*. The crystalline reference compounds were synthesized from the melanterite reagent for the purpose of this study.

is distinct from both, indicating that the arrangement of even these basic structural units may be different from those in the crystalline phases.

3.3. VNIR Spectroscopic Observations

VNIR spectra of amorphous sulfate samples are plotted along with several common sulfates in Figures 9, 11, and 12. The reference minerals were chosen to be the same as those used by *Cloutis et al.* [2008] in their study of sulfates at Mars-relevant temperatures and pressures. Also included are samples from *Lane et al.* [2015] that are spectrally similar to the amorphous ferric sulfate samples throughout this wavelength range. These reference samples have been investigated in detail in *Cloutis et al.* [2006, 2008], *Lane* [2007], and *Lane et al.* [2004, 2008, 2015]. The VNIR range for the ferric sulfates has been split into two regions: visible (VIS) (0.35–1.0 μm) and short wave infrared (SWIR) (0.90–2.5 μm) for easier visualization and discussion of electronic and vibrational features.

3.3.1. Amorphous Fe^{3+} Sulfates

In crystalline, Fe^{3+}-bearing minerals, absorptions due to spin-forbidden crystal field transitions of Fe^{3+}, are observed between 0.3 and 1 μm (Figure 9). When Fe^{3+} is linked through an oxygen or hydroxyl group, spin polarization and magnetic coupling remove degeneracy and lead to three common transitions: $^6A_{1g}$-($^4A_{1g}$,^4E_g), $^6A_{1g}$-$^4T_{2g}$, and $^6A_{1g}$-$^4T_{1g}$ [*Cloutis et al.*, 2006; *Rossman*, 1975]. In iron sulfates, these occur at ~0.43 μm, 0.5–0.6 μm, and 0.8–0.9 μm, respectively [*Cloutis et al.*, 2006], where oxo-bridged iron leads to deeper features than hydroxo-bridged iron [*Cloutis et al.*, 2006; *Sherman and Waite*, 1985]. The shape and position of these features relate to the distortion of the iron octahedra in the minerals [*Burns*, 1993; *Frost et al.*, 2005]. Through this wavelength range (~0.3–1.0 μm), the amorphous ferric sulfate sample spectra are distinct from the reference (crystalline sample) spectra. The absorptions due to Fe^{3+} spin-forbidden crystal field transitions are listed in Table 1 along with those values for

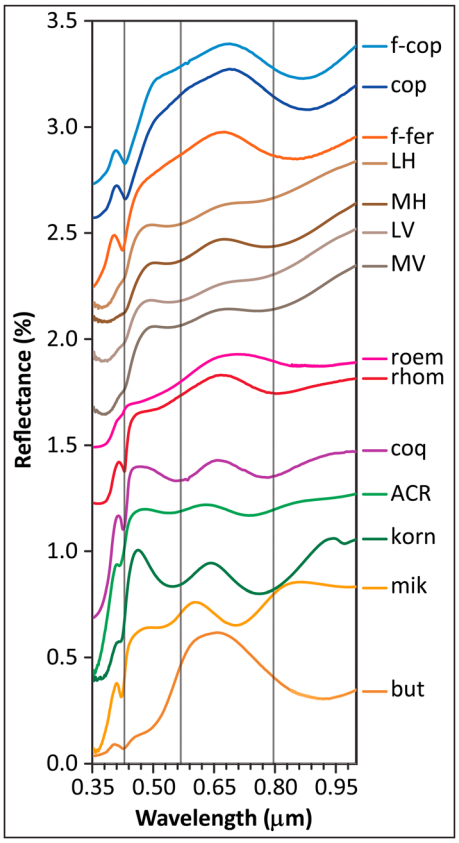

Figure 9. VIS spectra of (top to bottom) ferricopiapite (f-cop) ML-S35 (<125 μm), copiapite (cop) spt125 (<125 μm; 25% ferricopiapite), fibroferrite (f-fer) spt121 (<45 μm; 30% butlerite), LH-amorphous (LH) Fe^{3+} sulfate, MH-amorphous (MH) Fe^{3+} sulfate, LV-amorphous (LV) Fe^{3+} sulfate, MV-amorphous (MV) Fe^{3+} sulfate, römerite (roem) R8415 (<45 μm), rhomboclase (rhom) ML-S85 (<250 μm), coquimbite (coq) ML-S46 (<125 μm; subequal parts of coquimbite and paracoquimbite), Acros (ACR) starting material (XRD match to lausenite), kornelite (korn) ML-S105 (<45 μm), mikasaite (mik; the heated starting material), and butlerite (but) C5534 (<45 μm). Reference samples are from *Cloutis et al.* [2006, 2008], *Lane* [2007], and *Lane et al.* [2004, 2008, 2015] and are investigated in detail in those publications. Spectra are offset for clarity. Average positions of absorptions for the amorphous sulfates are shown with vertical lines.

several common sulfates from *Cloutis et al.* [2006] and *Lane et al.* [2015]. Noting that the position of the ^6A1_g-($^4A_{1g}$,^4E_g) of all the ferric sulfates are similar, the $^6A_{1g}$-$^4T_{2g}$ and the $^6A_{1g}$-$^4T_{1g}$ absorptions can be plotted in two dimensions to clarify the distinction in amorphous versus crystalline sample energies (Figure 10). It is clear from Figures 9 and 10 and Table 1 that the amorphous ferric sulfate absorption energies are very similar to coquimbite through the VIS. However, this trend does not continue into the SWIR (Figure 11), and both the absorption depths and overall spectral shape make the two minerals differentiable in the VIS.

In the SWIR wavelength region (Figure 11), H_2O-and OH-bearing sulfates show absorptions due to OH stretching overtones (~1.4 μm), overtones and combinations of structural H_2O (~1.4 μm), combinations of bending, stretching, and rotational features for OH and H_2O (~1.7–1.8 μm), H_2O combination modes (~1.9 μm), and combinations of bending, stretching, and rotational features for OH and H_2O along with S-O bending overtones (2.0–2.5 μm) [*Cloutis et al.*, 2006]. Spectrally, the amorphous ferric sulfates appear similar to other polyhydrated sulfate species reported by *Gendrin et al.* [2005], with broad, muted absorptions related to H_2O vibrational combination and overtone modes and S-O vibrational overtones. They have broad reflectance maxima at 1.14 μm, similar to ferricopiapite, and they also display weak doublets at 1.45 and 1.47 μm, broad absorptions at 1.73–1.77 μm, and broad, asymmetrical and strong absorptions centered at 1.95 μm. These samples lack distinct absorptions in the 2.0–2.4 μm region. The amorphous ferric sulfate spectra also show decreasing reflectance toward longer wavelengths (blue slope) past ~1.43 μm. The broadening and smearing of H_2O and OH features in materials is often seen when there is structural disorder or where there are many nonequivalent water sites. In these cases, the sloping spectrum indicates the overlap of a large number of H_2O and OH features [*Hunt*, 1977]. Among the synthesized amorphous samples measured, the slopes and positions of the absorptions through the SWIR are most similar to those in the reference spectra for (ferri)copiapite. Although all of the amorphous ferric sulfate samples share common features with many other sulfates, they do appear spectrally unique. The broad, smooth, and asymmetrical nature of the 1.9 μm hydration feature followed by the flat region spanning from 2.15 to 2.28 μm, the position and shape of the poorly defined 1.4 μm water feature, and the strong blue slope from 1.4 to 2.5 μm can be used to distinguish the amorphous sulfates from crystalline sulfate phases.

3.3.2. Amorphous Fe^{2+} Sulfate

The VNIR spectrum of the amorphous ferrous sulfate sample is shown in Figure 12. Unlike the amorphous ferric sulfates, the amorphous ferrous sulfate is dissimilar from common crystalline phases to which it is compared. It displays a reflectance maximum at 0.66 μm, a broad absorption at ~1.08 μm due to Fe^{2+} spin-allowed, crystal field transitions [*Crowley et al.*, 2003], and water combination bands at ~1.46 and

Table 1. Positions of the Ferric Iron Spin-Forbidden Crystal Field Transitions[a]

	$^6A_{1g}$-($^4A_{1g}$, ^4E_g)	$^6A_{1g}$-$^4T_{2g}$	$^6A_{1g}$-$^4T_{1g}$	Reference
Ferricopiapite	0.431	0.550	0.860–0.873	*Cloutis et al.* [2006]
(Ferri)Copiapite	0.430	0.535	0.885	*Lane et al.* [2015]
Fibroferrite	0.427	0.550	0.844	*Cloutis et al.* [2006]
LH amorphous	0.430	0.565	0.789	This study
MH amorphous	0.429	0.558	0.812	This study
LV amorphous	0.428	0.579	0.776	This study
MV amorphous	0.429	0.570	0.808	This study
Römerite	0.425	0.520	0.855	*Lane et al.* [2015]
Rhomboclase	0.430	0.525	0.800	*Lane et al.* [2015]
Coquimbite	0.430	0.560	0.785	*Lane et al.* [2015]
Acros (lausenite)	0.421	0.551	0.746	This study
Kornelite	0.421	0.550	0.766	*Lane et al.* [2015]
Mikasaite	0.424	0.535	0.709	This study
Butlerite	0.430	0.485	0.919	*Lane et al.* [2015]
Jarosite	0.435	0.665	0.905	*Lane et al.* [2015]

[a]All values are reported in microns. Exact positions were obtained for the amorphous samples, lausenite, mikasaite, and *Lane et al.* [2015] samples by performing a continuum removal in ENVI on the VNIR spectra. Exact positions for *Cloutis et al.* [2006] samples were taken directly from that paper. All samples are the same as those shown in Figures 9 and 11.

~1.95 μm. Although the water features are similar in position to those in melanterite, the amorphous sample displays only one iron absorption at 1.08 μm rather than the two seen in szomolnokite (~0.94 μm and ~1.33 μm), rozenite (~1.0 μm and ~1.2 μm), and melanterite (~0.88 μm and ~1.11 μm). Because the presence of the second Fe^{2+} crystal field absorption is caused by a distortion in the symmetry of the iron octahedral site [*Hunt*, 1977], the absence of a second absorption in the amorphous ferrous sulfate could indicate that the iron octahedra in the amorphous sulfate are less distorted than those in the crystalline sulfates.

3.4. MIR Emissivity Spectroscopic Observations

MIR emissivity spectra of iron sulfates are dominated by absorptions due to S-O vibrations in sulfate tetrahedra. The free sulfate anion has four vibrational modes: an asymmetric S-O stretch (ν_3; 1105 cm^{-1}), a symmetric S-O stretch (ν_1; 983 cm^{-1}), an asymmetric S-O-S bend (ν_4; 611 cm^{-1}), and a symmetric S-O-S bend (ν_2; 450 cm^{-1}) [*Lane*, 2007; *Nakamoto*, 1986]. In a free or undistorted sulfate polyhedron, only ν_3 and ν_4 are IR active, but when the sulfate anion is in a structure, it often distorts such that absorptions due to ν_1 and ν_2 are also visible. These distortions also affect the energy of the absorptions, making the MIR emissivity spectrum diagnostic [*Lane*, 2007]. Vibrational modes of the synthesized amorphous sulfates were assigned based on the similarity between the absorptions in the experimental spectrum and those reported for crystalline sulfates in *Lane* [2007] and *Lane et al.* [2015].

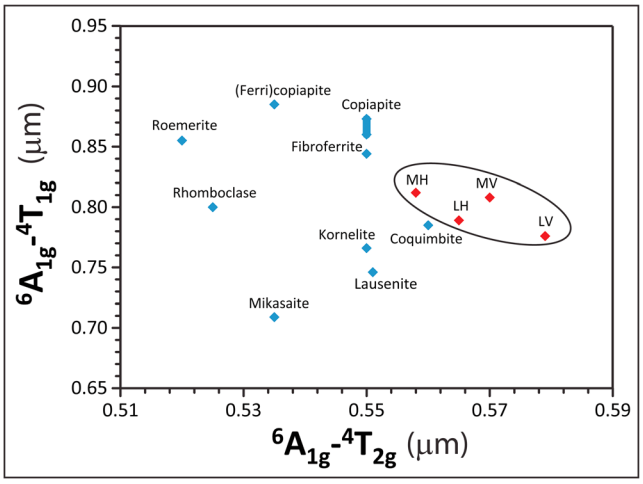

Figure 10. Plot of the VIS absorption positions for the $^6A_{1g}$-$^4T_{1g}$ versus the $^6A_{1g}$-$^4T_{2g}$ spin-forbidden crystal field transitions for the crystalline (blue) and amorphous (red) ferric sulfates listed in Table 1. Jarosite and butlerite fall well outside the plot.

3.4.1. Amorphous Fe^{3+} Sulfates

Emissivity spectra of pressed pellets of the amorphous ferric sulfates are plotted in Figure 13 along with emissivity spectra of pressed pellets of the Acros starting

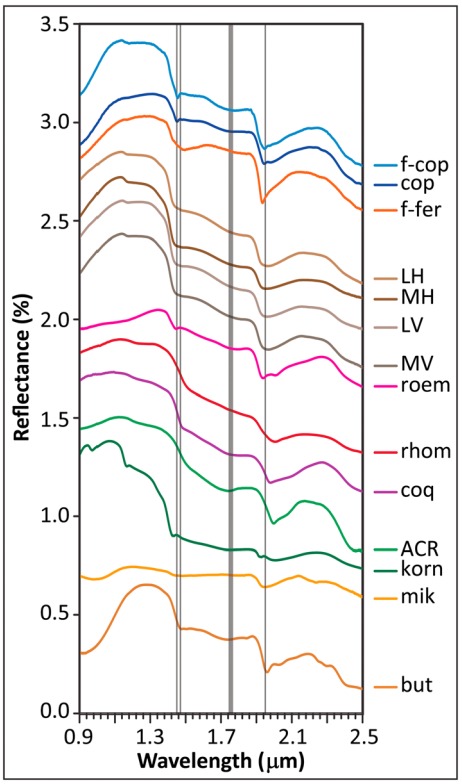

Figure 11. SWIR spectra of (top to bottom) ferricopiapite (f-cop) ML-S35 (<125 μm), copiapite (cop) spt125 (<125 μm; 25% ferricopiapite), fibroferrite (f-fer) spt121 (<45 μm; 30% butlerite), LH-amorphous (LH) Fe^{3+} sulfate, MH-amorphous (MH) Fe^{3+} sulfate, LV-amorphous (LV) Fe^{3+} sulfate, MV-amorphous (MV) Fe^{3+} sulfate, römerite (roem) R8415 (<45 μm), rhomboclase (rhom) ML-S85 (<250 μm), coquimbite (coq) ML-S46 (<125 μm; subequal parts of coquimbite and paracoquimbite) Acros (ACR) starting material (XRD match to lausenite), kornelite (korn) ML-S105 (<45 μm), mikasaite (mik; the heated starting material), and butlerite (but) C5534 (<45 μm). Reference samples are from *Cloutis et al.* [2006, 2008]; *Lane* [2007], and *Lane et al.* [2004, 2008, 2015] and are investigated in detail in those publications. Spectra are offset for clarity. Average positions of absorptions for the amorphous sulfates are shown with vertical lines.

material (XRD match to lausenite), the heated starting material (mikasaite), and a selection of crystalline ferric sulfates for which there were emissivity data from *Lane* [2007] and *Lane et al.* [2015]. Reference samples for the VNIR and MIR ranges are generally the same except for the absence of fibroferrite emissivity data and the inclusion of that for jarosite. Additional Fe^{2+}-bearing minerals were considered from those reported in *Lane et al.* [2015], like voltaite, römerite, and botryogen, but none of these minerals resemble the amorphous ferrous sulfate in the VNIR and were, therefore, not included in this paper. The amorphous ferric sulfates are all very similar, displaying three overlapping ν_3 bands at approximately 1203, 1112, and 1025 cm^{-1}, one ν_1 band at 989 cm^{-1}, two ν_4 bands at 650 and 588 cm^{-1}, and a ν_2 absorption around 455 cm^{-1} (denoted with vertical lines in Figure 13). The low-frequency ν_3 absorption and the ν_1 absorption are smoothed together in the vacuum dehydrated samples, whereas they are more distinct in the desiccated samples.

Based on the chemical formula and hydration state of the amorphous ferric samples (~6–8H_2O), the closest crystalline counterparts in Figure 13 are the Acros starting material (lausenite, $Fe(III)_2(SO_4)_3 \cdot 6H_2O$, "ACR"), kornelite ($Fe(III)_2(SO_4)_3 \cdot 7H_2O$), and (para)coquimbite ($Fe(III)_2(SO_4)_3 \cdot 9H_2O$). And although the amorphous ferric sulfate emissivity spectra do share similarities with the spectra for those three minerals, they are not a match through the whole frequency range, and the amorphous samples share features with many of the other minerals as well. The closest match in the reference samples considered is (para)butlerite VZO108 [*Lane et al.*, 2015], indicating that the energetic configuration of the sulfate anion in that sample may be similar to that for the amorphous ferric sulfates. However, the amorphous ferric sulfates are distinguishable from (para)butlerite through the shape of the band envelopes and the position of the ν_2 absorption at 455 cm^{-1}.

3.4.2. Amorphous Fe^{2+} Sulfates

An emissivity spectrum of a pressed pellet of the amorphous ferrous sulfate is plotted in Figure 14 along with emissivity spectra of pressed pellets of the melanterite starting material, rozenite, and szomolnokite. The szomolnokite reference sample is investigated in detail in *Lane et al.* [2015] and the rozenite reference sample is investigated in detail in *Bishop et al.* [2005] and *Lane et al.* [2015]. The amorphous ferrous sulfate displays two deep ν_3 bands at 1135 and ~1062 cm^{-1}, one ν_1 band at 970 cm^{-1}, one ν_4 band at 592 cm^{-1} with a shoulder at ~650 cm^{-1}, and two ν_2 bands at 455 and 441 cm^{-1}. These band positions are distinct from those of other ferrous sulfates. Based on chemical formula and hydration state, the closest crystalline counterpart to the amorphous ferrous sulfate is szomolnokite ($FeSO_4 \cdot H_2O$). Though the general ν_3 band envelope of the amorphous phase overlaps with szomolnokite, the specific band center positions are significantly shifted for all stretching and bending modes.

3.5. Mössbauer Spectroscopic Observations

3.5.1. Amorphous Fe^{3+} Sulfates

Mössbauer spectra of the amorphous ferric sulfates are shown in Figure 15, and the fit parameters are listed in Table 2. The spectra for the amorphous sulfates synthesized by all four formation pathways are similar. They

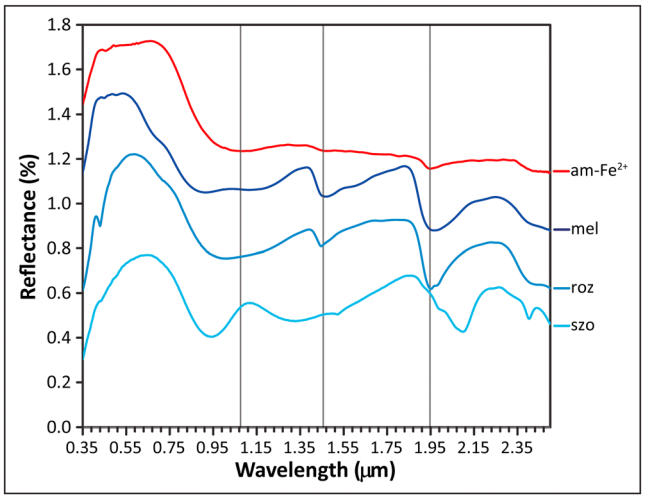

Figure 12. VNIR spectrum of vacuum-dehydrated, amorphous ferrous sulfate (am-Fe^{2+}) plotted with melanterite reagent (mel; phase confirmed by XRD directly prior to and after analysis), rozenite (roz) JB626B (<125 μm), and szomolnokite (szo) 104276 (<45 μm). The szomolnokite reference sample is investigated in detail in *Lane et al.* [2015], and the rozenite reference sample is investigated in detail in *Bishop et al.* [2005] and *Lane et al.* [2015]. Spectra are offset for clarity.

can all be fit with a single ferric doublet with an isomer shift of 0.44–0.45 mm/s, typical for ferric sulfates [*Dyar et al.*, 2013] (Table 2). The quadrupole splitting (Δ) values show more variation, with Δ for the hydration-dehydration samples ranging from 0.33–0.34 mm/s and Δ for the hydration-vacuum samples of 0.39 mm/s. The increase in quadrupole splitting for the vacuum-dehydrated samples indicates an increased distortion in the coordination polyhedron surrounding iron in those samples [*Burns and Solberg*, 1990; *Dyar et al.*, 2013]. An extensive study of the Mössbauer parameters of sulfates by *Dyar et al.* [2013] allows for the comparison of these values to those for many common sulfates (Figure 16). The amorphous ferric sulfate doublet is most similar to a doublet in (ferri)copiapite, halotrichite, voltaite, and römerite, which represent one of multiple nonequivalent iron sites in those minerals.

3.5.2. Amorphous Fe^{2+} Sulfates

The fitted Mössbauer spectrum for the amorphous ferrous sulfate is shown in Figure 17, and the fit parameters are listed in Table 2. The Mössbauer spectrum of the amorphous ferrous sulfate bears no similarity to any ferrous sulfate presented in the comprehensive study of iron sulfates by *Dyar et al.* [2013] (Figure 18). It can be fit with three overlapping doublets, all with isomer shift of 1.28–1.29 mm/s and quadrupole splitting values of 1.62, 2.24, and 2.73 mm/s. A distribution of doublets like this can indicate a range of nonequivalent sites, and the exact position of each doublet may not be conclusive for site identification purposes [*Eckert*, 1987]. However, it is worth noting that the doublet with the highest-velocity Δ value is a close match for that of several ferrous sulfates (Figure 18).

3.6. VNIR and MIR Characterization of Basalt—Amorphous Ferric Sulfate Mixtures

Because the amorphous ferric sulfates are formed through the dehydration of solutions, it is possible for them to form as cementing coatings on grains and as alteration products of deliquesced surface material. Here several experiments were performed where ~0.38 g of amorphous ferric sulfate was precipitated onto 0.50 g of terrestrial flood basalt sands (Wards Columbia River Plateau basalt; <63 μm grains; Figure 19, left inset). Optically, the amorphous ferric sulfates redden the surface of the basalt sands and the coated grains grind into a fine powder, visually similar to the ground unaltered basalt (Figure 19). When ground, it is expected that the sulfate and basalt act as an intimate mixture rather than individual-coated basalt grains because the sulfate is much softer than the basalt and would grind more readily. The spectra, however, are dominated by the spectrally opaque basalt rather than the sulfate (Figures 20 and 21); in particular, the 1.4 μm absorption is no longer visible, and the 1.9 and 2.5 μm absorptions are significantly dampened. Although the detection of these sulfates is clearly possible in the VNIR range, the discrimination of them from other polyhydrated phases may be challenging due to the spectral dominance of the basalt. In the MIR range, the presence of amorphous sulfate in a basalt mixture is most clearly observed in the spectral range between ~300 and 650 cm^{-1}; however, in general, the emissivity spectrum of the coated material is similar to that of the unaltered basalt.

Recently, *Masse et al.* [2014] investigated the spectral effects of coating basalts in brines at Mars relevant pressures and temperatures and tracked the spectral changes with dehydration. Although they started with anhydrous ferric sulfate, after hydrating and then dehydrating they also had a hydrated ferric sulfate species spectrally mixed with their basalt. We note that our basalt-amorphous sulfate mixture VNIR

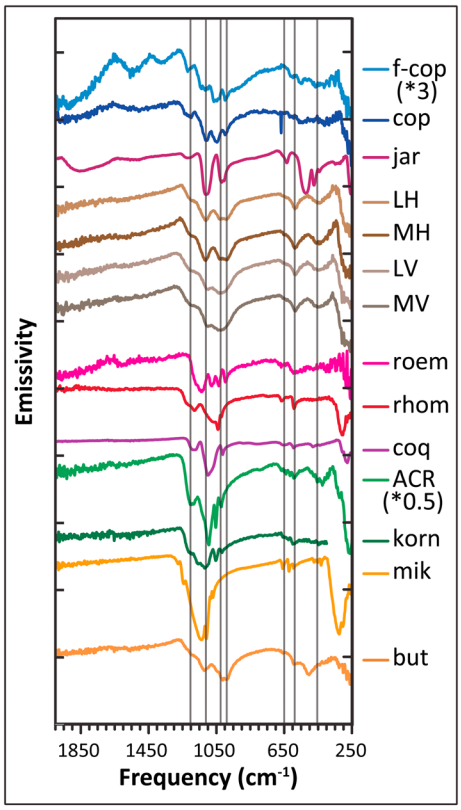

Figure 13. Emissivity spectra of (top to bottom) ferricopiapite (f-cop) ML-S35, copiapite (cop) spt125, jarosite (jar) ML-S51, LH-amorphous (LH) Fe^{3+} sulfate, MH-amorphous (MH) Fe^{3+} sulfate, LV-amorphous (LV) Fe^{3+} sulfate, MV-amorphous (MV) Fe^{3+} sulfate, römerite (roem) R8415, rhomboclase (rhom) ML-S85, coquimbite (coq) ML-S46, which is subequal parts of coquimbite and paracoquimbite, Acros (ACR) starting material (XRD match to lausenite), kornelite (korn) ML-S105, mikasaite (mik; the heated starting material), and butlerite (but) VZO108. All samples are in the form of pressed powder pellets. Reference samples are from *Lane* [2007] and *Lane et al.* [2015] and are investigated in detail in those publications. Spectra are offset for clarity. Average positions of absorptions for the amorphous sulfate are shown with vertical lines.

spectrum (Figure 20) bears a striking similarity to the end product observed by *Masse et al.* [2014] (their Figure 6a). *Masse et al.* [2014] did not acquire XRD data for their end product, but based on our experiments, it seems possible that the sulfate phase left on their basalt was amorphous and that the amorphous phase is to be expected at Mars-relevant temperatures and pressures.

4. Discussion

4.1. Structural and Spectral Comparison to Crystalline Iron Sulfates

Each analysis technique used in this study provides different yet complementary information about the sample structures. Mössbauer data provide information about the number of nonequivalent iron sites in the structure, the valence state of iron in those sites, the coordination of iron in those sites (based on the value of the isomer shift), and information about the distortion of those sites (based on the quadrupole splitting value). PDF data provide short- and medium-range structural details through mapping the atomic pair correlations in the structure but require modeling and comparison to reference structures for more complete structural characterization. VIS data provide information pertaining to the energy of the Fe^{3+} spin-forbidden crystal field transitions [*Hunt*, 1977], and because these transitions arise from the magnetic coupling of linked octahedra [*Sherman et al.*, 1982], they are more sensitive to longer-range structure, specifically along oxo- and hydroxo-bridged M-ligand units [*Rossman*, 1975]. Therefore, the VIS data may indicate structural differences not seen at the level of individual octahedra and, therefore, not as readily apparent from the Mössbauer data. Thermal infrared (TIR) absorptions arise from vibrational frequencies associated with molecular bending, stretching, and translation, which are affected by bond lengths and angles. Thus, the TIR data are sensitive to both short- and long-range structures.

4.1.1. Amorphous Fe^{3+} Sulfates

The Mössbauer parameters for the amorphous ferric sulfates are very close to those for one of multiple doublets in halotrichite, römerite, voltaite, and (ferri) copiapite (Figure 17), indicating that the distortion of the coordination polyhedron around Fe^{3+} in the amorphous ferric sulfates is likely similar to the distortion in these minerals. In the MIR (Figure 13), despite the chemical and hydration state similarity to lausenite, kornelite, and (para)coquimbite, the band envelopes and positions of the ν_3, ν_1, and ν_4 absorptions most closely match (para)butlerite (VZO108) from *Lane et al.* [2015]. While the energetic environment of the sulfate anion is similar to (para) butlerite, the energetic environment of the iron octahedra are clearly distinct, displaying much lower Δ values than those typical for (para)butlerite of 0.96–0.99 mm/s. PDF data (Figures 6 and 7) for the amorphous ferric sulfate samples show these materials only possess structural order to about 10 Å. The short-range order (to ~ 4.5 Å) is similar to all the ferric sulfates, indicating that over those length scales, there are limited energetically favorable configurations (bond lengths) for iron octahedra and sulfate tetrahedra. Past 5 Å, the amorphous samples no longer resemble any of the crystalline reference compounds. The position of the absorptions from the Fe^{3+} spin-forbidden crystal field transitions (Figures 9 and 10) observed in the VIS data also indicate that the amorphous ferric sulfate samples show

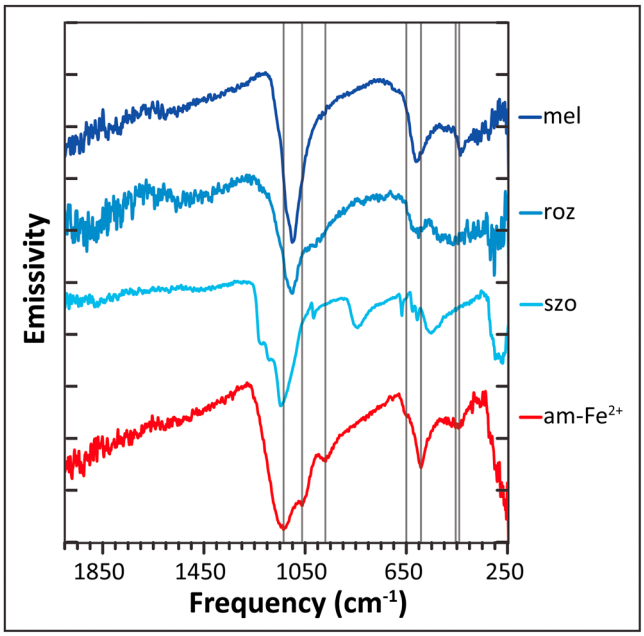

Figure 14. Emissivity spectra of (top to bottom) melanterite starting material (mel; phase confirmed by XRD directly prior to and after analysis), rozenite (roz) JB626B, szomolnokite (szo) 104276, and vacuum-dehydrated, amorphous ferrous sulfate (am-Fe^{2+}). All samples were in the form of pressed powder pellets. The szomolnokite reference sample is investigated in detail in *Lane et al.* [2015], and the rozenite reference sample is investigated in detail in *Bishop et al.* [2005] and *Lane et al.* [2015]. Spectra are offset for clarity. Average positions of absorptions for the amorphous sulfate are shown with vertical lines.

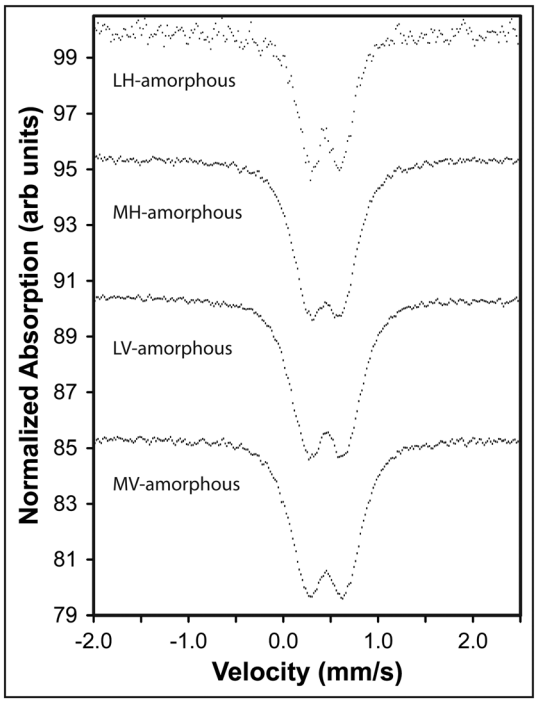

Figure 15. Mössbauer spectra of amorphous ferric sulfates taken at 295 K. Spectra are scaled and offset for clarity.

distinct longer-range structure. Generally, the absorption from the Fe^{3+} $^6A_{1g}$-$^4T_{1g}$ spin-forbidden transition (Figure 10, *y* axis) occurs at higher wavelengths for hydroxo-bridged minerals than for oxo-bridged minerals, with the highest values corresponding to minerals with the most extensive networks of hydroxo-bridged octahedra [*Rossman*, 1975, 1976]. The opposite trend can be seen for the absorption from the Fe^{3+} $^6A_{1g}$-$^4T_{2g}$ spin-forbidden transition (Figure 10, *x* axis); here higher values (in wavelength space) correspond to minerals with less extensive octahedral linkages, such that absorption from the hydroxo-bridged dimers in copiapite is greater than that for the hydroxo-bridged chains of octahedra in botryogen or butlerite [*Rossman*, 1975, 1976]. Given these general trends, the amorphous ferric sulfates' VIS absorptions are most consistent with oxo-bridged, clusters—possibly dimers, octahedra that bridge through sulfate groups like coquimbite, or isolated octahedra (with or without bonds to sulfate tetrahedra) like römerite and halotrichite. PDF data on additional ferric sulfates of different base structural units are required for a more complete structural analysis.

4.1.2. Amorphous Fe^{2+} Sulfates

The Mössbauer spectrum for the amorphous ferrous sulfate is unlike any crystalline ferrous sulfate reviewed by *Dyar et al.* [2013]. However, the parameters of the doublet with the highest-velocity Δ are quite close to those for römerite, szomolnokite, and halotrichite (Figure 18). The parameters with the lowest velocity Δ are closest, although not a match, to one doublet in voltaite. Mössbauer parameter similarities are not, however, unique enough to draw structural conclusions in the absence of other evidence [*Dyar et al.*, 2013]. Multiple overlapping doublets in the Mössbauer fit can indicate a range of nonequivalent sites for iron rather than energetically similar but distinct sites. It is interesting, however, that the amorphous ferrous sulfates have a significant doublet with Δ between 1.9 and 2.7 mm/s since no other sulfates investigated by *Dyar et al.* [2013] have a significant doublet in that range (Figure 18).

The VNIR spectrum of the amorphous ferrous sulfate only displays a single absorption from the spin allowed $E_g \rightarrow T_{2g}$ Fe^{2+} crystal field transition

Table 2. Mössbauer Fit Parameters for the Amorphous Iron Sulfates

Sample	Site	δ	Δ	Γ	%Area	χ^2
Amorphous ferrous sulfate	1	1.29	1.62	0.51	31	6.5
	2	1.28	2.24	0.44	39	
	3	1.28	2.73	0.40	29	
LH amorphous	1	0.45	0.33	0.29	100	1.3
MH amorphous	1	0.44	0.34	0.38	100	2.0
LV amorphous	1	0.45	0.39	0.40	100	3.6
MV amorphous	1	0.45	0.39	0.40	100	2.7

(Figure 12). Melanterite, rozenite, and szomolnokite all display two absorptions, which are common for minerals where octahedral distortion has caused further splitting of the energy levels [*Hunt*, 1977]. Although the hydration state of the amorphous ferrous sulfate is closest to szomolnokite, the positions of water-related absorptions through the NIR occur at similar positions to those for rozenite and melanterite but are much shallower than those for the similarly hydrated szomolnokite sample.

As with the Mössbauer and VNIR data, the MIR data support the unique structural nature of the amorphous ferrous sulfate (Figure 14). The general ν_3 band envelope overlaps with szomolnokite (which has a similar hydration state to the amorphous phase), but features within that envelope, and all other vibrational features throughout the MIR, are significantly shifted from szomolnokite and the other crystalline phases used for comparison. Further work to characterize this structure is currently underway.

The PDF data (Figure 8) for the amorphous ferrous sulfates do show some short- and medium-range (<6 Å) similarities with both szomolnokite and rozenite but also some differences. For instance, the peak attributed to the Fe-O distance is slightly different in all three samples as well as the O-O distances in sulfate. Differences are also evident in the region near 4 Å, where Fe-O distances occur in szomolnokite, but at a greater distance in rozenite. These data, like the Mössbauer, VNIR, and MIR data, suggest that although the local structure of the amorphous ferrous sulfate shares some similarities with the reference compounds, it is certainly not the same. More work is needed to determine the specific short- and medium-range structures for this sample.

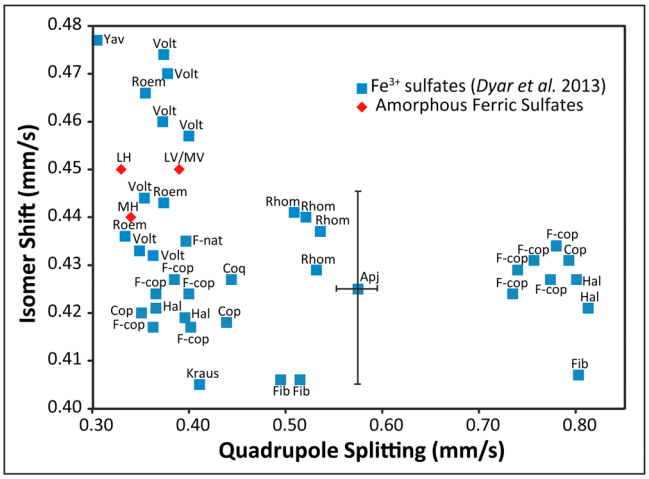

Figure 16. Isomer shift versus quadrupole splitting for amorphous ferric sulfates plotted with Fe^{3+} sulfate doublets from *Dyar et al.* [2013] that have quadrupole splitting of 0.31–0.80 mm/s. Abbreviations are as follows: apjohnite (Apj), copiapite (Cop), ferricopiapite (F-cop), ferrinatrite (F-nat), fibroferrite (Fib), halotrichite (Hal), krausite (Kraus), rhomboclase (Rhom), römerite (Roem), voltaite (Volt), yavapaiite (Yav), LH-amorphous (LH), MH-amorphous (MH), LV-amorphous (LV), and MV-amorphous (MV). Errors for all data points are the same as those shown for apjohnite.

4.2. Effects of Dehydration Method and Starting Material on Amorphous Phase Characteristics

Based on our experimental investigations and accounts in the literature, amorphous ferric sulfates thus far have only been formed from dehydration of saturated solutions, whereas amorphous ferrous sulfates have only been formed from dehydration of highly hydrated crystalline phases [*Wang and Zhou*, 2014; *Wang et al.*, 2012; *Xu and Parise*, 2012; *Xu et al.*, 2009]. Despite current efforts from these experiments and those of other authors [*Wang and Zhou*, 2014], amorphous ferrous sulfates have not been successfully precipitated from brines, and they go through crystalline phases (usually rozenite followed by melanterite) before deliquescence.

The starting materials used for synthesis of the amorphous ferric sulfates have

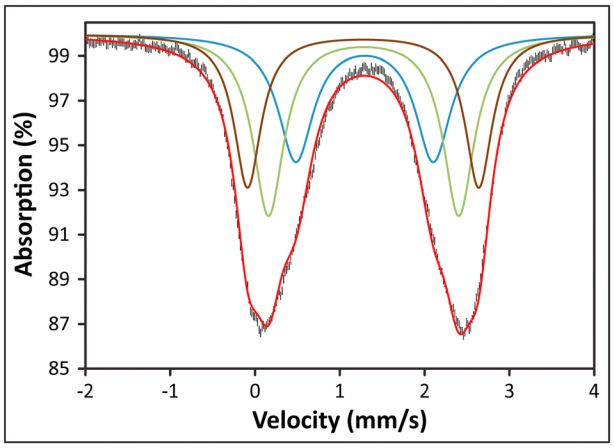

Figure 17. Mössbuaer spectrum of amorphous ferrous sulfate taken at 295 K. Three distributions and total fit are overlayed on the spectrum.

little effect on the structure of the amorphous phase. The observed structural similarities between amorphous samples synthesized from different starting materials are not unexpected because both starting materials deliquesce at 92% relative humidity, producing similar saturated brines. Although the starting material had little effect on the amorphous product, the method of dehydration did have a small influence on the Mössbauer quadrupole-splitting parameter and the MIR emissivity spectra. The vacuum-dehydrated samples have a higher quadrupole-splitting (Δ) value than those dehydrated using buffering salts (section 3.5). The increase in Δ indicates an increase in the distortion of the iron octahedron [*Burns and Solberg*, 1990; *Dyar et al.*, 2013]. The MIR emissivity spectra also show slight differences due to the method of dehydration. The ν_3 and ν_1 absorptions are smoothed together in the vacuum-dehydrated samples but are better defined in the samples dehydrated using RH buffering salts (section 3.4). In the MIR, broadening features also indicate structural disorder, since a given absorption may occur over a greater range of energies, indicating a range of configurations and coordinations within the solid [*Farmer*, 1974; *Lane*, 2007]. The increased disorder for the vacuumed samples, observed in the MIR and Mössbauer data, is likely due to the relative rate of water loss; the vacuumed samples, which dehydrate more quickly, have a greater degree of disorder.

4.3. A Case for Amorphous Iron Sulfates on Mars

Recent results from the Mars Science Laboratory's (MSL) analysis of the Rocknest Soil at Gale Crater have added valuable information to our understanding of the Martian surface sediments. The soil at Rocknest was analyzed by ChemMin and SAM (Sample Analysis at Mars) providing XRD and evolved gas analysis (EGA) data. Those analyses, reported in a series of papers by the science team [*Archer et al.*, 2014; *Bish et al.*, 2013; *Blake et al.*, 2013; *Dehouck et al.*, 2014; *Leshin et al.*, 2013; *McAdam et al.*, 2014], estimated that at least 20 wt % and possibly up to 45 wt % of the Rocknest soil is XRD-amorphous material. EGA results showed high levels of evolved H_2O and SO_2; the temperature at which some of the sulfate evolved is consistent with Fe sulfates (too low for Ca and Mg sulfates) [*McAdam et al.*, 2014], yet no evidence for Fe sulfates, or any hydrated sulfate, was found by ChemMin in the crystalline portion of the Rocknest soil [*Bish et al.*, 2013; *McAdam et al.*, 2014]. Rather, the evolved H_2O and SO_2 gas (upon heating) likely originated from the XRD amorphous component of the soil [*Leshin et al.*, 2013; *McAdam et al.*, 2014]. *McAdam et al.* [2014] interpret the iron in the amorphous portion to

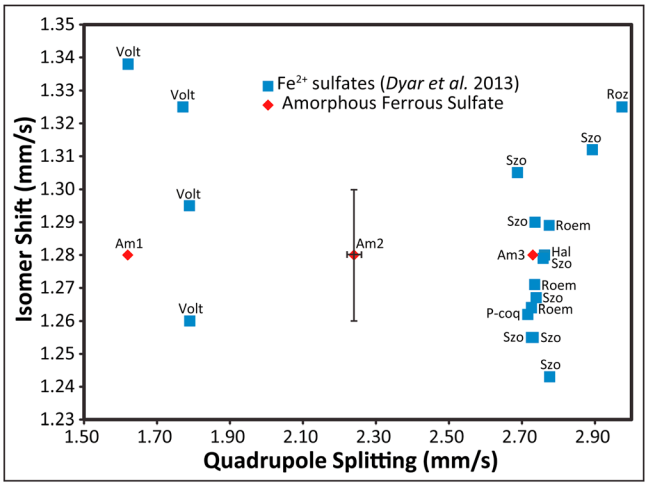

Figure 18. Isomer shift versus quadrupole splitting for amorphous ferric sulfates plotted with Fe^{2+} sulfate doublets from *Dyar et al.* [2013]. Abbreviations are as follows: halotrichite (Hal), paracoquimbite (P-coq), römerite (Roem), szomolnokite (Szo), voltaite (Volt), and amorphous ferrous sulfate doublets 1 (Am1), 2 (Am2), and 3 (Am3). Errors for all data points are the same as those shown for Am2.

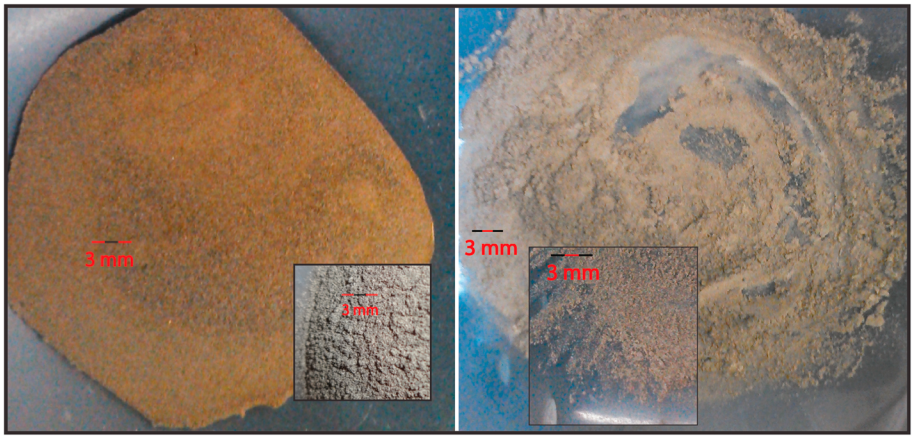

Figure 19. Image of MH-amorphous precipitated onto <63 μm flood basalt (left) unground and (right) ground. The inset on the right shows the ground, uncoated flood basalt. The inset on the left shows the unground, uncoated flood basalt.

be likely present as nanophase iron oxide (XRD amorphous) and interpret the sulfate to be present as a sulfate anion adsorbed onto the surface of other XRD amorphous phases, such as allophane or nanophase iron oxide.

An alternative explanation for the recent Rocknest findings could be that some of the evolved SO_2 and H_2O have come from amorphous Fe sulfates. Under conditions of high relative humidity (likely present in the shallow subsurface [*Wang et al.*, 2013]), crystalline ferric sulfates would deliquesce. Then, once brought to low relative humidity (e.g., through excavation or brine flow), rapid dehydration would lead to structural disorder, thus forming amorphous ferric sulfates. Their ability to change hydration state without crystallizing increases their potential longevity in the Martian climate. Under the ambient laboratory conditions in State University of New York at Stony Brook's geology department (23°C, 14%RH), the amorphous samples can remain XRD amorphous for several days. The low temperatures of the Martian surface and subsurface would retard the crystallization of these phases, because the activation energy may not be available for a change of structure. Therefore, it is likely that the daily Martian RH fluctuations would result in hydration and dehydration of the amorphous phase but not necessarily induce crystallization. And thus it would be possible for them to become incorporated into the regolith.

More broadly, evidence for a present-day brine hydrologic cycle suggests that amorphous sulfates could be present in soil as brine evaporative products in a more widespread fashion. Ferric sulfate brines have a eutectic temperature of 205 K, which would allow them to form anywhere on the Martian surface and over much of the Martian shallow subsurface [*Chevrier and Altheide*, 2008; *Karunatillake et al.*, 2009]. Because amorphous ferric sulfates are formed directly from the saturated fluid, evaporation or boiling of these brines has the potential to deposit amorphous ferric sulfates on the Martian surface. Ferrous sulfate brines, on the other hand, have a relatively high eutectic temperature of 267.2 K [*Altheide et al.*, 2009], and, as described in section 4.2, a brine dehydration scenario would not likely lead to amorphous ferrous sulfates. Although amorphous ferrous sulfates may form on Mars through the exposure of higher hydrates to lower RH conditions

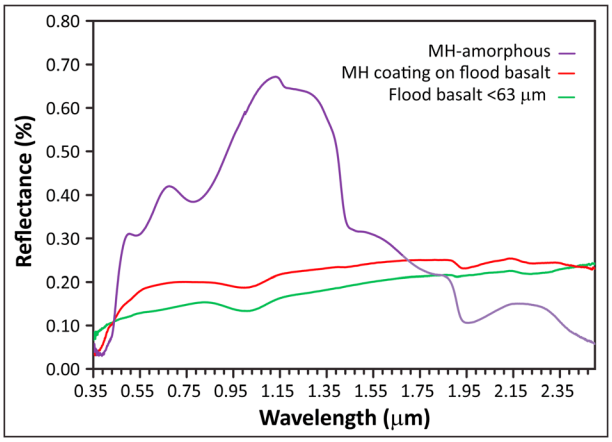

Figure 20. VNIR spectra of MH-amorphous ferric sulfate, MH-amorphous ferric sulfate precipitated onto <63 μm flood basalt and <63 μm uncoated flood basalt.

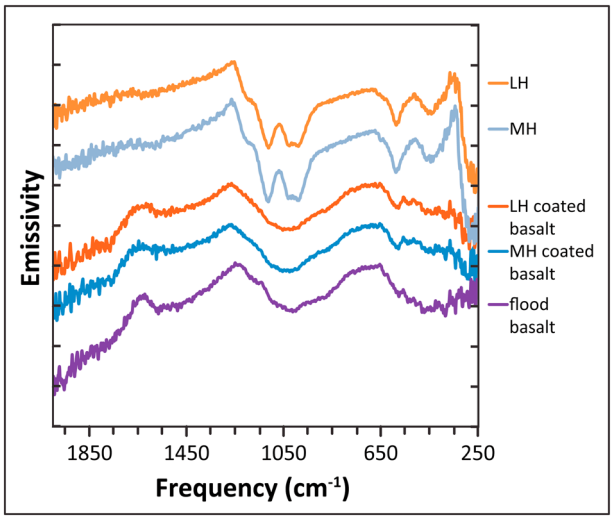

Figure 21. Emissivity spectra of (top to bottom) LH-amorphous ferric sulfate, MH-amorphous ferric sulfate, LH-amorphous ferric sulfate precipitated onto <63 μm basalt, MH-amorphous precipitated onto < 63 μm basalt, and < 63 μm flood basalt. All samples were measured as pressed powder pellets. Spectra are offset for clarity.

through processes that bring material from the subsurface to the surface, it is unlikely that we will detect them because amorphous ferrous sulfates are found to oxidize and/or recrystallize quite rapidly.

Globally, water-equivalent hydrogen values as high as 15 wt % at the equator [*Feldman et al*., 2004; *Maurice et al*., 2011] have led authors to speculate how that water is stabilized in the shallow subsurface under present Martian conditions. Of the candidate mechanisms, which include subsurface H_2O ice, adsorbed water on dust, hydrous salts other than sulfates, and moderately to highly hydrated sulfates, only the latter explanation meets the requirements for stability and realistic abundance in the shallow subsurface [*Wang et al*., 2013]. In addition, the Mars Odyssey Gamma Ray Spectrometer (GRS) provided H:S ratios that are most consistent with hydrated iron sulfates with between ~2.5 and ~4 structural waters per sulfate [*Karunatillake et al*., 2014]. Amorphous ferric sulfates remain consistent with GRS data, as these phases can hold between 1.7 and 3.7 structural waters per sulfate (5–11 waters per $Fe_2(SO_4)_3$ [*Wang et al*., 2012]), although mixtures of higher and lower hydrates are possible.

If these amorphous ferric sulfates were present on Mars at Gale Crater, what percentage of the soil could they account for? Using estimates of H_2O abundance in Rocknest soils from the SAM instrument (1.5–3.0 wt % H_2O) [*Leshin et al*., 2013], as well as estimates of abundance (30–45 wt %) and the H_2O-free chemical composition of the amorphous portion of Rocknest [*Dehouck et al*., 2014, Table 3], we can calculate an upper limit for abundance of amorphous ferric sulfate at Gale Crater (Table S1 in the supporting information). First, because no hydrous crystalline phases were identified in Rocknest with CheMin [*Bish et al*., 2013], we can assume that all of the H_2O detected by SAM came from the amorphous portion of the soil. Using the lower *Dehouck et al*. [2014] estimate of 30 wt % amorphous material in the soil, H_2O would make up 5–10 wt % of the amorphous component; for 45 wt % amorphous material, H_2O comprises 3.3–6.7 wt % of the amorphous component. Next, using the stoichiometry for lausenite ($Fe_2(SO_4)_3 \cdot 6H_2O$) as a proxy for the amorphous ferric sulfate (section 3), we can calculate the amount of FeOT and SO_3 in the amorphous portion of Rocknest that is used when all of the H_2O is placed in the amorphous ferric sulfate phase. For example, using the entire 5 wt % H_2O (for the case where amorphous components comprise 30 wt% of Rocknest), amorphous ferric sulfate uses ~6.6 wt % FeOT and ~11.1% SO_3, making up a total of ~22.7 wt % of the amorphous fraction or ~6.8 wt % of bulk Rocknest. The amount of FeOT and SO_3 used do not exceed the available amounts estimated for amorphous component bulk composition ([*Dehouck et al*., 2014, Table 3] renormalized to 95 wt % to account for 5 wt % H_2O); thus, the calculated abundance is plausible. For 10 wt % H_2O, it is not possible to use the entire H_2O budget in the amorphous phase because there is not enough SO_3 to create the correct stoichiometry. Exhausting the SO_3 budget for this phase alone (which seems unlikely), the amorphous ferric sulfate would make up 29.6 wt % of the amorphous component (using 6.5 wt % of the available 10.0 wt % H_2O) or 8.9 wt % of the total soil. Using the higher *Dehouck et al*. [2014] estimate of 45 wt % amorphous material in the soil, and assuming all the H_2O came the amorphous phase (now ~3.3–6.7 wt % H_2O in the amorphous component), an upper estimate of ferric sulfate abundance can be determined. The abundance of amorphous ferric sulfate that uses up the entire 3.3 wt % H_2O is 15.0 wt % of the amorphous component or 6.8 wt % of the total soil. For 6.7 wt % H_2O, it is again not possible to use the entire H_2O budget, but exhausting the SO_3 budget leads to an amorphous ferric sulfate abundance 20.9 wt % of the amorphous component (using 4.6 wt % H_2O) or

9.4 wt % of the total soil. In summary, amorphous ferric sulfates could comprise between ~6.8–9.4 wt % of the bulk Rocknest soil (Table S1), assuming that the amount of hydration is similar to that of lausenite ($Fe_2(SO_4)_3 \cdot 6H_2O$). Higher hydration states are possible, and the amorphous sulfate could hold up to 11 structural H_2O [*Wang et al.*, 2012]. However, our calculated abundances are relatively insensitive to hydration state. For example, increasing the hydration from 6 to 8 H_2O per $Fe_2(SO_4)_3$ changes the range of bulk abundances from ~6.8–9.4 wt % to ~6.7–9.3 wt %. Thus, our estimates remain robust within the constraints provided by the MSL data.

The spectral characterizations reported in this study indicate that NIR absorptions associated with amorphous sulfates are muted and broadened compared to their crystalline counterparts (Figures 11, 12, and 20), and thus could go undetected in remote measurements of intimate soil mixtures, especially at levels below 10 wt % as may be the case for Gale Crater. If present in high concentrations in outcrops or mixed with spectrally transparent materials, however, the spectral details in the VIS, NIR, and MIR ranges should allow them to be distinguished from crystalline sulfates.

5. Summary and Conclusions

Our ability to accurately interpret the surface mineralogy of Mars is directly dependent upon the breadth of the library to which we compare Martian spectra. Here that library is expanded to include VNIR, MIR emissivity, and Mössbauer spectra of synthetic, amorphous ferric, and ferrous sulfates. We also evaluated the likelihood of these phases being present on Mars, based on our work and synthesis of the literature, and conclude that amorphous ferric phases could be common in Martian soils.

From this work, we have determined the following:

1. Amorphous ferric sulfates, and ferric sulfates in general, exhibit path-dependent transformations. Although ferrous sulfates can reversibly change hydration states, as well as crystallinity, while remaining solid, amorphous ferric sulfates seem only to result from the rapid dehydration of a fully deliquesced crystalline sulfate or an iron and sulfate-saturated fluid [also see *Wang and Ling*, 2011]. If amorphous ferric sulfates were discovered on Mars, a combination of hydration, followed by rapid dehydration, would be implied. We thus may be able to use them to place constraints not only on the fluids from which they formed, and surface conditions on Mars at the time of formation, but also atmospheric conditions at the time of formation.
2. Amorphous ferric sulfates only show structural order extending to ~10 Å, with short-range structures similar to crystalline ferric sulfates to ~4 Å. Amorphous ferric sulfates have Mössbauer parameters similar to one doublet of (ferri)copiapite, voltaite, and halotrichite, indicating similar iron octahedral distortion to one of the sites in those minerals. In the MIR, spectral features are broadened and muted compared to crystalline ferric sulfate phases; however, the positions of the major bands of the amorphous ferric phases coincide closely with those of butlerite, indicating similar energetic environments around sulfate in the two minerals.
3. Amorphous ferric sulfates form spectrally similar products regardless of the starting materials we used; however, subtle spectral differences are observed with different formation pathways. The vacuum dehydrated samples display greater iron site distortion (have a higher velocity Mössbauer Δ), along with a smoothing together of their MIR low-frequency ν_3 absorption and their ν_1 absorption not seen in desiccated samples; this is likely due to the higher speed of water loss associated with the vacuum dehydration method.
4. Visible reflectance spectra show the amorphous ferric sulfates to be distinct from crystalline ferric sulfates based on the position of their spin-forbidden crystal field transition absorptions. The position of those absorptions may indicate that the basic structural units of the amorphous ferric sulfates are oxo-bridged iron octahedral clusters, octahedra connected through sulfate tetrahedral, or isolated octahedral units.
5. The amorphous ferric sulfates display broadened and weakened hydration features in SWIR reflectance spectra. Though similar to other polyhydrated crystalline sulfates in this wavelength range, the amorphous ferric sulfates are spectrally distinct from other ferric sulfates in the spectral library in the region of the 1.9 μm absorption.
6. Amorphous ferrous sulfate lacks structural order beyond ~11 Å and has a local structural environment that shares some features with szomolnokite and rozenite but is distinct in other features.

7. Consistent with structural information obtained from total X-ray scattering data, amorphous ferrous sulfate is spectrally distinct from all other ferrous sulfates available for comparison based on Mössbauer, VNIR, and MIR spectra. The amorphous ferrous sulfate displays one rather than two Fe^{2+} spin-allowed crystal field transition absorptions in the VNIR. In the MIR, the ν_3 band envelope overlaps with that of szomolnokite, but features within that envelope are significantly shifted, indicating that the sulfate tetrahedral environment is distinct from that of the reference compounds.
8. Rapid dehydration of $Fe(III)_2(SO_4)_3$-saturated fluids leads to formation of amorphous ferric sulfate phases. This, combined with evidence for a present-day brine hydrologic cycle [e.g., *McEwen et al*., 2014], suggests that amorphous sulfates could be present in soil as brine evaporative products. Their ability to change hydration state without crystallizing increases their potential longevity in the Martian climate. Under the ambient laboratory conditions (23°C, 14%RH), the amorphous samples can remain XRD amorphous for several days. We suggest that the low temperatures of the Martian surface and subsurface would further slow the crystallization of these phases. Daily Martian RH fluctuations would result in hydration and dehydration of the amorphous phases but not necessarily induce crystallization. Thus, we conclude that there is a high likelihood that these phases could be incorporated into the Martian regolith.
9. If present in Gale Crater soils (Rocknest), amorphous ferric sulfate phases could comprise between ~6.8 and 9.4 wt % of the bulk soil or ~15–30% of the amorphous fraction of the soil. This would account for most or all of the H_2O and SO_3, and ~10–30% of the FeO in the amorphous fraction of the soil.

Acknowledgments
This work was funded by the NASA Planetary Geology and Geophysics Program, under grant NNX12AO45G to A.D.R. and R.J.R. This research used resources of the Advanced Photon Source, a U.S. Department of Energy (DOE) Office of Science User Facility operated for the DOE Office of Science by Argonne National Laboratory under contract DE-AC02-06CH11357. Mössbauer spectra were kindly provided by Mount Holyoke's Mössbauer Spectroscopy Lab. We are grateful to Melissa Lane and our anonymous reviewer for the thorough and useful suggestions contained in their reviews. All spectral data collected as part of this work will be available at http://aram.ess.sunysb.edu/drogers upon acceptance of this publication.

References

Altheide, T., V. Chevrier, C. Nicholson, and J. Denson (2009), Experimental investigation of the stability and evaporation of sulfate and chloride brines on Mars, *Earth Planet. Sci. Lett.*, *282*(1–4), 69–78, doi:10.1016/j.epsl.2009.03.002.

Archer, P. D., et al. (2014), Abundances and implications of volatile-bearing species from evolved gas analysis of the Rocknest aeolian deposit, Gale Crater, Mars, *J. Geophys. Res. Planets*, *119*, 237–254, doi:10.1002/2013JE004493.

Audouard, J., F. Poulet, M. Vincendon, R. E. Milliken, D. Jouglet, J. P. Bibring, B. Gondet, and Y. Langevin (2014), Water in the Martian regolith from OMEGA/Mars Express, *J. Geophys. Res. Planets*, *119*, 1969–1989, doi:10.1002/2014JE004649.

Baldridge, A. M., and P. R. Christensen (2009), A laboratory technique for thermal emission measurement of hydrated minerals, *Appl. Spectrosc.*, *63*(6), 678–688.

Bigham, J. M., U. Schwertmann, L. Carlson, and E. Murad (1990), A poorly crystallized oxyhydroxysulfate of iron formed by bacterial oxidation of Fe(II) in acid mine waters, *Geochim. Cosmochim. Acta*, *54*, 2743–2758.

Billinge, S. L., and M. G. Kanatzidis (2004), Beyond crystallography: The study of disorder, nanocrystallinity and crystallographically challenged materials with pair distribution functions, *Chem. Commun.*, *7*, 749–760, doi:10.1039/B309577K.

Bish, D. L., et al. (2013), X-ray diffraction results from mars science laboratory: Mineralogy of Rocknest at Gale Crater, *Science*, *341*(6153), doi:10.1126/science.1238932.

Bishop, J. L., M. D. Dyar, M. D. Lane, and J. F. Banfield (2005), Spectral identification of hydrated sulfates on Mars and comparison with acidic environments on Earth, *Int. J. Astrobiol.*, *3*, 275–285, doi:10.1017/S1473550405002259.

Bishop, J. L., et al. (2009), Mineralogy of Juventae Chasma: Sulfates in the light-toned mounds, mafic minerals in the bedrock, and hydrated silica and hydroxylated ferric sulfate on the plateau, *J. Geophys. Res.*, *114*, E00D09, doi:10.1029/2009JE003352.

Blake, D. F., et al. (2013), Curiosity at Gale Crater, Mars: Characterization and analysis of the Rocknest sand shadow, *Science*, *341*(6153), doi:10.1126/science.1239505.

Brass, G. W. (1980), Stability of brines on Mars, *Icarus*, *42*(1), 20–28, doi:10.1016/0019-1035(80)90237-7.

Burgina, E. B., G. N. Kustova, S. G. Nikitenko, D. I. Kochubei, and G. L. Elizarova (1996), A comparative study of some basic iron(III) sulfates, *J. Struct. Chem.*, *37*(2), 240–246.

Burns, R. G. (1993), Origin of electronic spectra of minerals in the visible-near infrared region, in *Remote Geochemical Analysis: Elemental and Mineralogical Composition*, edited by C. M. Pieters and P. A. J. Englert, pp. 3–29, Cambridge Univ. Press, Cambridge, U. K.

Burns, R. G., and T. C. Solberg (1990), ^{57}Fe-bearing oxide, silicate, and aluminosilicate minerals, crystal structure trends in Mössbauer spectra, in *Spectroscopic Characterization of Minerals and Their Surfaces*, *Am. Chem. Soc. Symp. Ser.*, vol. 415, pp. 262–283, American Chemical Society, Washington, D. C.

Chevrier, V. F., and T. S. Altheide (2008), Low temperature aqueous ferric sulfate solutions on the surface of Mars, *Geophys. Res. Lett.*, *35*, L22101, doi:10.1029/2008GL035489.

Chevrier, V., D. W. G. Sears, J. D. Chittenden, L. A. Roe, R. Ulrich, K. Bryson, L. Billingsley, and J. Hanley (2007), Sublimation rate of ice under simulated Mars conditions and the effect of layers of mock regolith JSC Mars-1, *Geophys. Res. Lett.*, *34*, L02203, doi:10.1029/2006GL028401.

Chou, I. M., R. R. Seal II, and A. Wang (2013), The stability of sulfate and hydrated sulfate minerals near ambient conditions and their significance in environmental and planetary sciences, *J. Asian Earth Sci.*, *62*, 734–758, doi:10.1016/j.jseaes.2012.11.027.

Cloutis, E. A., et al. (2006), Detection and discrimination of sulfate minerals using reflectance spectroscopy, *Icarus*, *184*(1), 121–157, doi:10.1016/j.icarus.2006.04.003.

Cloutis, E. A., M. A. Craig, R. V. Kruzelecky, W. R. Jamroz, A. Scott, F. C. Hawthorne, and S. A. Mertzman (2008), Spectral reflectance properties of minerals exposed to simulated Mars surface conditions, *Icarus*, *195*(1), 140–168, doi:10.1016/j.icarus.2007.10.028.

Crowley, J. K., D. E. Williams, J. M. Hammarstrom, N. Piatak, I. M. Chou, and J. C. Mars (2003), Spectral reflectance properties (0.4–2.5 μm) of secondary Fe-oxide, Fe-hydroxide, and Fe-sulfate-hydrate minerals associated with sulphide-bearing mine wastes, *Geochem. Explor. Environ. Anal.*, *3*(3), 219–228, doi:10.1144/1467-7873/03-001.

Degrave, E., and A. Vanalboom (1991), Evaluation of ferrous and ferric Mössbauer fractions, *Phys. Chem. Miner.*, *18*(5), 337–342.

Dehouck, E., S. M. McLennan, P. Y. Meslin, and A. Cousin (2014), Constraints on abundance, composition and nature of X-ray amorphous components of soils and rocks at Gale Crater, Mars, *J. Geophys. Res. Planets*, *119*, 2640–2657, doi:10.1002/2014JE004716.

Dyar, M. D., et al. (2013), Mössbauer parameters of iron in sulfate minerals, *Am. Mineral.*, *98*(11–12), 1943–1965, doi:10.2138/am.2013.4604.
Eckert, H. (1987), Mössbauer spectroscopy of mixed-valence compounds, in *Mössbauer Spectroscopy of Inorganic Compounds*, edited by G. L. Long, 125 pp., Springer, New York.
Farmer, V. C. (1974), *Infrared Spectra of Minerals*, 539 pp., Mineralogical Society, London.
Feldman, W. C., et al. (2004), Global distribution of near-surface hydrogen on Mars, *J. Geophys. Res.*, *109*, E09006, doi:10.1029/2003JE002160.
Frost, R. L., R. A. Wills, W. Martens, M. Weier, and B. J. Reddy (2005), NIR spectroscopy of selected iron(II) and iron(III) sulphates, *Spectrochim. Acta, Part A*, *62*(1–3), 42–50, doi:10.1016/j.saa.2004.12.003.
Gendrin, A., et al. (2005), Sulfates in Martian layered terrains: The OMEGA/Mars Express view, *Science*, *307*(5715), 1587–1591, doi:10.1126/science.1109087.
Golden, D. C., D. W. Ming, R. V. Morris, and S. A. Mertzman (2005), Laboratory-simulated acid-sulfate weathering of basaltic materials: Implications for formation of sulfates at Meridiani Planum and Gusev Crater, Mars, *J. Geophys. Res.*, *110*, E12S07, doi:10.1029/2005JE002451.
Harri, A. M., et al. (2014), Mars Science Laboratory relative humidity observations: Initial results, *J. Geophys. Res. Planets*, *119*, 2132–2147, doi:10.1002/2013JE004514.
Hawthorne, F. C., S. V. Krivovichev, and P. C. Burns (2000), The crystal chemistry of sulfate minerals, *Rev. Mineral. Geochem.*, *40*, 1–112, doi:10.2138/rmg.2000.40.1.
Hunt, G. R. (1977), Spectral signatures of particulate minerals in the visible and near IR, *Geophysics*, *42*(3), 501–513, doi:10.1190/1.1440721.
Johnson, J. R., J. F. Bell III, E. Cloutis, M. Staid, W. H. Farrand, T. McCoy, M. Rice, A. Wang, and A. Yen (2007), Mineralogic constraints on sulfur-rich soils from Pancam spectra at Gusev Crater, Mars, *Geophys. Res. Lett.*, *34*, L13202, doi:10.1029/2007GL029894.
Karunatillake, S., J. J. Wray, S. W. Squires, G. J. Taylor, O. Gasnault, S. M. McLennan, W. Boyton, M. R. El Maarry, and J. M. Dohm (2009), Chemically striking regions on Mars and Stealth revisited, *J. Geophys. Res.*, *114*, E12001, doi:10.1029/2008JE003303.
Karunatillake, S., J. J. Wray, O. Gasnault, S. M. McLennan, A. D. Rogers, S. W. Squyres, W. V. Boynton, J. R. Skok, L. Ojha, and N. Olsen (2014), Sulfates hydrating bulk soil in the Martian low and middle latitudes, *Geophys. Res. Lett.*, *41*, 7987–7996, doi:10.1002/2014GL061136.
King, P. L., and H. Y. McSween Jr. (2005), Effects of H_2O, pH, and oxidation state on the stability of Fe minerals on Mars, *J. Geophys. Res.*, *110*, E12S10, doi:10.1029/2005JE002482.
King, P. L., D. T. Lescinsky, and H. W. Nesbitt (2004), The composition and evolution of primordial solutions on Mars, with application to other planetary bodies, *Geochim. Cosmochim. Acta*, *68*(23), 4992–5008, doi:10.1016/j.gca.2004.05.036.
Knowlton, G. D., T. R. White, and H. L. McKague (1981), Thermal study of types of water associates with clinoptilolite, *Clays Clay Miner.*, *29*(5), 403–411.
Kong, W. G., A. Wang, and I. M. Chou (2011a), Experimental determination of the phase boundary between kornelite and pentahydrated ferric sulfate at 0.1 MPa, *Chem. Geol.*, *284*(3–4), 333–338, doi:10.1016/j.chemgeo.2011.03.014.
Kong, W. G., A. Wang, J. J. Freeman, and P. Sobron (2011b), A comprehensive spectroscopic study of synthetic Fe^{2+}, Fe^{3+}, Mg^{2+} and Al^{3+} copiapite by Raman, XRD, LIBS, MIR and VIS-NIR, *J. Raman Spectrosc.*, *42*(5), 1120–1129, doi:10.1002/jrs.2790.
Lane, M. D. (2007), Mid-infrared emission spectroscopy of sulfate and sulfate-bearing minerals, *Am. Mineral.*, *92*(1), 1–18, doi:10.2138/am.2007.2170.
Lane, M. D., M. D. Dyar, and J. L. Bishop (2004), Spectroscopic evidence for hydrous iron sulfate in the Martian soil, *Geophys. Res. Lett.*, *31*, L19702, doi:10.1029/2004GL021231.
Lane, M. D., J. L. Bishop, M. D. Dyar, P. L. King, M. Parente, and B. C. Hyde (2008), Mineralogy of the Paso Robles soils on Mars, *Am. Mineral.*, *93*, 728–739, doi:10.2138/am.2008.2757.
Lane, M. D., J. L. Bishop, M. D. Dyar, T. Hiroi, S. A. Mertzman, D. L. Bish, P. L. King, and A. D. Rogers (2015), Mid-infrared emission spectroscopy and visible/near-infrared reflectance spectroscopy of Fe-sulfate minerals, *Am. Mineral.*, *100*, 66–82, doi:10.2138/am-2015-4762.
Lazaroff, N., W. Signal, and A. Wasserman (1982), Iron Oxidation and precipitation of ferric hydroxysulfates by resting *Thiobacillus-Ferrooxidans* cells, *Appl. Environ. Microbiol.*, *43*(4), 924–938.
Lazaroff, N., L. Melanson, E. Lewis, N. Santoro, and C. Pueschel (1985), Scanning electron-microscopy and infrared-spectroscopy of iron sediments formed by *Thiobacillus-Ferrooxidans*, *Geomicrobiol. J.*, *4*(3), 231–268.
Lazaroff, N., J. Jollie, and P. R. Dugan (1998), Amorphous hydrated Fe(III) sulfate: Metastable product and bio-geochemical marker of iron oxidizing Thiobacilli, in *Proceedings of the Society of Photo-Optical Instrumentation Engineers, Conference Instruments, Methods, and Missions for Astrobiology*, vol. 3441, edited by R. B. Hoover, pp. 264–279, San Diego, Calif., doi:10.1117/12.319853.
Leshin, L. A., et al. (2013), Volatile, isotope, and organic analysis of Martian fines with the Mars Curiosity rover, *Science*, *341*(6153), doi:10.1126/science.1238937.
Lichtenberg, K. A., et al. (2010), Stratigraphy of hydrated sulfates in the sedimentary deposits of Aram Chaos, Mars, *J. Geophys. Res.*, *115*, E00D17, doi:10.1029/2009JE003353.
Ling, Z. C., and A. Wang (2010), A systematic spectroscopic study of eight hydrous ferric sulfates relevant to Mars, *Icarus*, *209*(2), 422–433, doi:10.1016/j.icarus.2010.05.009.
Majzlan, J., and R. Michallik (2007), The crystal structures, solid solutions and infrared spectra of copiapite-group minerals, *Mineral. Mag.*, *71*(5), 553–569, doi:10.1180/minmag.2007.071.5.553.
Majzlan, J., C. Boetez, and P. W. Stephens (2005), The crystal structures of synthetic Fe2(SO4)3(H2O)5 and the type of specimen lausenite, *Am. Mineral.*, *90*, 411–416, doi:10.2138/am.2005.1701.
Majzlan, J., A. Navrotskly, R. B. McCleskey, and C. N. Alpers (2006), Thermodynamic properties and crystal structure refinement of ferricopiapite, coquimbite, rhomboclase, and $Fe_2(SO_4)_3(H_2O)_5$, *Eur. J. Mineral.*, *18*, 175–186, doi:10.1127/0935-1221/2006/0018-0175.
Margulis, E. V., L. A. Savchenko, M. M. Shokarev, L. I. Beisekeeva, and F. I. Vershinina (1975), Amorphic basic sulfate 2Fe2O3.SO3.MH2O, *Zh. Neorg. Khim.*, *20*(7), 1872–1875.
Margulis, E. V., L. S. Getskin, N. A. Zapuskalova, and F. I. Vershinina (1976), Concentration conditions for formation of primary crystalline and amorphous phases during hydrolytic precipitation of iron (III) from sulfate solutions, *J. Appl. Chem. USSR*, *49*(11), 2383–2387.
Marion, G. M., D. C. Catling, and J. S. Kargel (2003), Modeling aqueous ferrous iron chemistry at low temperatures with application to Mars, *Geochim. Cosmochim. Acta*, *67*(22), 4251–4266, doi:10.1016/S0016-7037(03)00372-7.
Martinez, G. M., and N. O. Renno (2013), Water and brines on Mars: Current evidence and implications for MSL, *Space Sci. Rev.*, *175*(1–4), 29–51, doi:10.1007/s11214-012-9956-3.
Masse, M., P. Beck, B. Schmitt, A. Pommerol, A. McEwen, V. Chevrier, O. Brissaud, and A. Sejourne (2014), Spectroscopy and detectability of liquid brines on Mars, *Planet. Space Sci.*, *92*, 136–149, doi:10.1016/j.pss.2014.01.018.
Maurice, S., W. Feldman, B. Diez, O. Gasnault, D. J. Lawrence, A. Pathare, and T. Prettyman (2011), Mars Odyssey neutron data: 1. Data processing and models of water-equivalent-hydrogen distribution, *J. Geophys. Res.*, *116*, E11008, doi:10.1029/2011JE003810.

McAdam, A. C., et al. (2014), Sulfur-bearing phases detected by evolved gas analysis of the Rocknest aeolian deposit, Gale Crater, Mars, *J. Geophys. Res. Planets*, *119*, 373–393, doi:10.1002/2013JE004518.
McCord, T. B., G. Teeter, G. B. Hansen, M. T. Sieger, and T. M. Orlando (2002), Brines exposed to Europa surface conditions, *J. Geophys. Res.*, *107*(E1), 5004, doi:10.1029/2000JE001453.
McEwen, A. S., L. Ojha, C. M. Dundas, S. S. Mattson, S. Byrne, J. J. Wray, S. C. Cull, S. L. Murchie, N. Thomas, and V. C. Gulick (2011), Seasonal flows on warm Martian slopes, *Science*, *333*(6043), 740–743, doi:10.1126/science.1204816.
McEwen, A. S., C. M. Dundas, S. S. Mattson, A. D. Toigo, L. Ojha, J. J. Wray, M. Chojnacki, S. Byrne, S. L. Murchie, and N. Thomas (2014), Recurring slope linae in equitorial regions of Mars, *Nat. Geosci.*, *7*, 53–58, doi:10.1038/NGEO2014.
Milliken, R. E., and D. L. Bish (2010), Sources and sinks of clay minerals on Mars, *Philos. Mag.*, *90*(17–18), 2293–2308, doi:10.1080/14786430903575132.
Milliken, R. E., W. W. Fischer, and J. A. Hurowitz (2009), Missing salts on early Mars, *Geophys. Res. Lett.*, *36*, L11202, doi:10.1029/2009GL038558.
Mohlmann, D., and K. Thomsen (2011), Properties of cryobrines on Mars, *Icarus*, *212*(1), 123–130, doi:10.1016/j.icarus.2010.11.025.
Nakamoto, K. (1986), *Infrared and Raman Spectra of Inorganic and Coordinated Compounds*, Wiley, New York.
Reeder, R. J., and F. M. Michel (2013), Application of total X-ray scattering methods and pair distribution function analysis for study of structure of biominerals, in *Research Methods in Biomineralization Science*, edited by J. J. D. Yoreo, pp. 477–500, Waltham, Mass.
Roach, L. H., J. F. Mustard, S. L. Murchie, J. P. Bibring, F. Forget, K. W. Lewis, O. Aharonson, M. Vincendon, and J. L. Bishop (2009), Testing evidence of recent hydration state change in sulfates on Mars, *J. Geophys. Res.*, *114*, E00D02, doi:10.1029/2008JE003245.
Roach, L. H., J. F. Mustard, M. D. Lane, J. L. Bishop, and S. L. Murchie (2010a), Diagenetic haematite and sulfate assemblages in Valles Marineris, *Icarus*, *207*(2), 659–674, doi:10.1016/j.icarus.2009.11.029.
Roach, L. H., J. F. Mustard, G. Swayze, R. E. Milliken, J. L. Bishop, S. L. Murchie, and K. Lichtenberg (2010b), Hydrated mineral stratigraphy of Ius Chasma, Valles Marineris, *Icarus*, *206*(1), 253–268, doi:10.1016/j.icarus.2009.09.003.
Rossman, G. R. (1975), Spectroscopic and magnetic studies of ferric iron hydroxy sulfates-intensification of color in ferric iron clusters bridged by a single hydroxide ion, *Am. Mineral.*, *60*(7–8), 698–704.
Rossman, G. R. (1976), Spectroscopic and magnetic studies of ferric iron hydroxy sulfates-series Fe(OH)SO4.nH2O and jarosites, *Am. Mineral.*, *61*(5–6), 398–404.
Ruff, S. W., P. R. Christensen, P. W. Barbera, and D. L. Anderson (1997), Quantitative thermal emission spectroscopy of minerals: A laboratory technique for measurement and calibration, *J. Geophys. Res.*, *102*(B7), 14,899–14,913, doi:10.1029/97JB00593.
Salisbury, J. W., and A. E. Wald (1992), The role of volume scattering in reducing spectral contrast of reststrahlen bands in spectra of powdered minerals, *Icarus*, *96*, 121–128, doi:10.1016/0019-1035(92)90009-V.
Savijarvi, H. (1995), Mars boundary-layer modeling—Diurnal moisture cycle and soil properties at the Viking-Lander-1 site, *Icarus*, *117*(1), 120–127, doi:10.1006/icar.1995.1146.
Sears, D. W. G., and J. D. Chittenden (2005), On laboratory simulation and the temperature dependence of the evaporation rate of brine on Mars, *Geophys. Res. Lett.*, *32*, L23203, doi:10.1029/2005GL024154.
Shepard, M. K., and P. Helfenstein (2007), A test of the Hapke photometric model, *J. Geophys. Res.*, *112*, E03001, doi:10.1029/2005JE002625.
Sherman, D. M., and T. D. Waite (1985), Electronic-spectra of Fe3+ oxides and oxide hydroxides in the near IR to near UV, *Am. Mineral.*, *70*(11–12), 1262–1269.
Sherman, D. M., R. G. Burns, and V. M. Burns (1982), Spectral characteristics of the iron-oxides with application to the Martian bright region mineralogy, *J. Geophys. Res.*, *87*(NB12), 169–180, doi:10.1029/JB087iB12p10169.
Squyres, S. W., et al. (2004), In situ evidence for an ancient aqueous environment at Meridiani Planum, Mars, *Science*, *306*(5702), 1709–1714, doi:10.1126/science.1104559.
Tosca, N. J., S. M. McLennan, D. H. Lindsley, and M. A. A. Schoonen (2004), Acid-sulfate weathering of synthetic Martian basalt: The acid fog model revisited, *J. Geophys. Res.*, *109*, E05003, doi:10.1029/2003JE002218.
Vandenberghe, R. E., E. De Grave, and P. M. A. de Bakker (1994), On the methodology of the analysis of Mössbauer spectra, *Hyperfine Interact.*, *83*(1), 29–49, doi:10.1007/BF02074257.
Vaniman, D. T., and S. J. Chipera (2006), Transformations of Mg- and Ca-sulfate hydrates in Mars regolith, *Am. Mineral.*, *91*(10), 1628–1642, doi:10.2138/am.2006.2092.
Vaniman, D. T., D. L. Bish, S. J. Chipera, C. I. Fialips, J. W. Carey, and W. C. Feldman (2004), Magnesium sulphate salts and the history of water on Mars, *Nature*, *431*(7009), 663–665, doi:10.1038/nature02973.
Wang, A., and Z. C. Ling (2011), Ferric sulfates on Mars: A combined mission data analysis of salty soils at Gusev Crater and laboratory experimental investigations, *J. Geophys. Res.*, *116*, E00F17, doi:10.1029/2010JE003665.
Wang, A., J. J. Freeman, B. L. Jolliff, and I. M. Chou (2006a), Sulfates on Mars: A systematic Raman spectroscopic study of hydration states of magnesium sulfates, *Geochim. Cosmochim. Acta*, *70*(24), 6118–6135, doi:10.1016/j.gca.2006.05.022.
Wang, A., et al. (2006b), Sulfate deposition in subsurface regolith in Gusev Crater, Mars, *J. Geophys. Res.*, *111*, E02S17, doi:10.1029/2005JE002513.
Wang, A., J. J. Freeman, and B. L. Jolliff (2009), Phase transition pathways of the hydrates of magnesium sulfate in the temperature range 50 degrees C to 5 degrees C: Implication for sulfates on Mars, *J. Geophys. Res.*, *114*, E04010, doi:10.1029/2008JE003266.
Wang, A., J. J. Freeman, I. M. Chou, and B. L. Jolliff (2011), Stability of Mg-sulfates at −10 degrees C and the rates of dehydration/rehydration processes under conditions relevant to Mars, *J. Geophys. Res.*, *116*, E12006, doi:10.1029/2011JE003818.
Wang, A., W. C. Feldman, M. T. Mellon, and M. P. Zheng (2013), The preservation of subsurface sulfates with mid-to-high degree of hydration in equatorial regions on Mars, *Icarus*, *226*(1), 980–991, doi:10.1016/j.icarus.2013.07.020.
Wang, A. A., and Y. H. Zhou (2014), Experimental comparison of the pathways and rates of the dehydration of Al-, Fe-, Mg- and Ca-sulfates under Mars relevant conditions, *Icarus*, *234*, 162–173, doi:10.1016/j.icarus.2014.02.003.
Wang, A. A., Z. C. Ling, J. J. Freeman, and W. G. Kong (2012), Stability field and phase transition pathways of hydrous ferric sulfates in the temperature range 50 degrees C to 5 degrees C: Implication for Martian ferric sulfates, *Icarus*, *218*(1), 622–643, doi:10.1016/j.icarus.2012.01.003.
Wiseman, S. M., R. E. Arvidson, R. V. Morris, F. Poulet, J. C. Andrews-Hanna, J. L. Bishop, S. L. Murchie, F. P. Seelos, D. Des Marais, and J. L. Griffes (2010), Spectral and stratigraphic mapping of hydrated sulfate and phyllosilicate-bearing deposits in northern Sinus Meridiani, Mars, *J. Geophys. Res.*, *115*, E00D18, doi:10.1029/2009JE003354.
Wray, J. J., et al. (2011), Columbus crater and other possible groundwater-fed paleolakes of Terra Sirenum, Mars, *J. Geophys. Res.*, *116*, E01001, doi:10.1029/2010JE003694.
Xu, W., and J. B. Parise (2012), Temperature and humidity effects on ferric sulfate stability and phase transformation, *Am. Mineral.*, *97*(2–3), 378–383, doi:10.2138/am.2012.3927.
Xu, W. Q., N. J. Tosca, S. M. McLennan, and J. B. Parise (2009), Humidity-induced phase transitions of ferric sulfate minerals studied by in situ and ex situ X-ray diffraction, *Am. Mineral.*, *94*(11–12), 1629–1637, doi:10.2138/am.2009.3182.